Tectonophysics 896 (2025) 230607

Contents lists available at ScienceDirect

Tectonophysics

journal homepage: www.elsevier.com/locate/tecto

Factors affecting the Pacific plate subduction towards and under the Changbaishan volcanic province since the Cenozoic: Insights from geodynamic modeling based on data assimilation

Tao Zhu [a,b,*], Diandian Peng [c], Lijun Liu [d]

[a] Institute of Geophysics, China Earthquake Administration, Beijing 100081, China
[b] Beijing Baijiatuan Earth Sciences National Observation and Research Station, Beijing 100095, China
[c] Scripps Institution of Oceanography, UC San Diego, La Jolla, CA 92093, USA
[d] State Key Laboratory of Lithospheric Evolution, Institute of Geology and Geophysics, Chinese Academy of Sciences, Beijing 100029, China

ARTICLE INFO

Keywords:
Slab subduction
Geodynamic modeling
Pacific plate
Model parameter
Slab dynamics

ABSTRACT

The origin of the Changbaishan volcanic province (CVP) has been considered to correlate with the subduction of the Pacific plate, so it is necessary to dynamically reconstruct the subduction history of the Pacific plate towards and beneath the CVP since the Cenozoic for probing the mechanism of the CVP. Many parameters affect slab subduction dynamics, so how to choose these parameters reasonably is the urgent issue to be solved during the reconstruction. A lot of analogue and numerical models have been used to study the effects of these parameters, but almost all of them have not considered a slab subduction history. In addition, seismic tomographic models have manifested that there is a high-speed anomaly zone extending over 1300 km within the mantle transition zone (MTZ) beneath the CVP. The zone is belived to consist of the Pacific slab in its eastern part and a segment of delaminated continental lithosphere (DCL) in its western part, bounded by approximately 120°E. A reasonable geodynamic model should reproduce both the Pacific slab and the DCL. Accordingly, in order to provide a reference for selecting geodynamic model parameters, we initially develop a series of three-dimensional (3D) thermochemical geodynamic models with data assimilation, in which several parameters are varied independently. These parameters encompass the Clapeyron slopes (γ_{410} and γ_{660}) and thicknesses (δh_{410} and δh_{660}) of the 410-km and 660-km discontinuities, the viscosities in the lower mantle (η_{lw}), the mantle transition zone (η_{mtz}) and the middle part of the lower mantle (η_{mlw}), seafloor age (t_o), the densities of the oceanic crust (representing it with the buoyancy ratio B_6) and asthenosphere ($\Delta\rho_{asth}$), as well as the density jump across the 660-km discontinuity ($\Delta\rho_{660}$). Subsequently, we primarily investigate how these parameters influence the westward movement distance, sinking depth, and structure of the Pacific slab, as well as whether geodynamic models incorporating these parameters can predict the high-speed anomaly zone. Finally, for reasonably reproducing the Pacific slab and the DCL beneath the CVP, we propose a suggested range of these parameters: γ_{660} may lie within the range of −2.0 to −3 MPa/K; η_{lw} and η_{mlw} may range from 30 to 50 and should not exceed 75; B_6 may be set to −0.48, which corresponds to a mean density of 3.0 g/cm^3 for the Earth's oceanic crust; the lower limit of the t_o may be adopted; η_{mtz} may be 1.0 to 2.5; $\Delta\rho_{asth}$ should adopt a reasonable and more negative value; and $\Delta\rho_{660}$ may be set to a value of 10 to 15 %.

1. Introduction

The Changbaishan volcanic province, comprising the volcanoes of Tianchi, Paotaishan and Wangtian'e, is situated in the border region between China and North Korea (Fig. 1). These volcanoes have erupted vigorously numerous times since the Miocene era and have been experiencing unrest in the last 20 years, thus posing a risk of potentially disastrous eruptions (Liu et al., 2015; Acocella et al., 2015; Wei et al., 2013; Xu et al., 2012; Hong et al., 2007; Wu et al., 2007). The origin of the CVP is complex, and so far, three main conceptual models/mechanisms have been proposed, inferred from seismic and geochemical results. The three models/mechanisms are related to the deep dehydration

* Corresponding author at: Institute of Geophysics, China Earthquake Administration, Beijing 100081, China.
E-mail addresses: zhutao@cea-igp.ac.cn, zxl_tao@126.com (T. Zhu).

https://doi.org/10.1016/j.tecto.2024.230607
Received 14 August 2024; Received in revised form 6 November 2024; Accepted 15 December 2024
Available online 19 December 2024

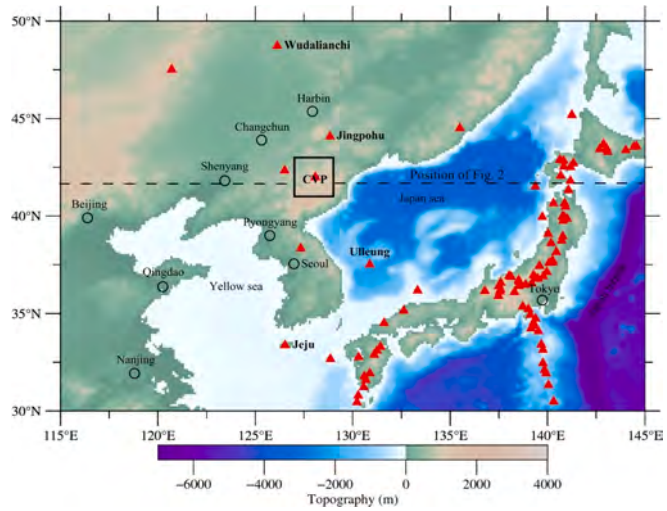

Fig. 1. Location of the Changbaishan volcanic province (CVP). The red triangles stand for volcanoes. (For interpretation of the references to colour in this figure legend, the reader is referred to the web version of this article.)

of a stagnant Pacific slab in the MTZ, the piling up and thickening of a stagnant Pacific slab in the MTZ, and the upward escape of oceanic asthenosphere material entrained by the subducting Pacific slab through slab gaps in the MTZ (Du and Lei, 2019; Guo et al., 2018; Chen et al., 2017; Zhao et al., 2017; Tian et al., 2016; Wei et al., 2015; Liu and Zhou, 2015; Tang et al., 2006, 2014; Lei et al., 2013). All three mechanisms highlight the importance of Pacific plate subduction. Consequently, a reasonable reconstruction of the Pacific slab subduction history is conducive to probing deeply into the origin of the CVP.

Numerous analogue and numerical simulations have demonstrated that multiple parameters affect slab subduction dynamics. These parameters include the rheology of the subduction interface; the thickness, density, rheology, chemical composition, length, and width of the subducting slab; the thickness, density, and rheology of the overriding slab; the duration of subduction; the viscosity and density of the mantle; trench retreat velocity; and the properties of upper-mantle seismic discontinuities (Christensen, 1996; Bina et al., 2001; Kincaid and Griffiths, 2003; Funiciello et al., 2006; Stegman et al., 2010; Capitanio and Faccenda, 2012; Sharples et al., 2014; Chertova et al., 2018; Sheng et al., 2018; Li et al., 2014, 2019a; Hu and Gurnis, 2020; Király et al., 2020; Xue et al., 2020; Zhong and Li, 2020; Peng et al., 2021a; Behr et al., 2022; Chen et al., 2022). These simulations shed light on the general understanding of slab subduction dynamics. For instance, convergence speeds, subducting plate velocities and trench retreat rates increase with decreasing viscosity at the subduction interface. Particularily, a decrease in viscosity by ~2 orders of magnitude can lead to an increase in convergence speeds by ~1 order of magnitude (Androvičová et al., 2013; Čížková and Bina, 2013; Ratnaswamy et al., 2015; Pokorny et al., 2021; Behr et al., 2022). The larger the trench retreat rate, the smaller the dip angle of a subducting slab (e.g., Griffiths et al., 1995). Consequently, the greater the probability of the slab stagnating in the MTZ, meaning that it becomes more difficult for the slab to penetrate the 660-km discontinuity and enter the lower mantle (e.g., Crameri and Lithgow-Bertelloni, 2018; Zhong and Gurnis, 1997; Kincaid and Olson, 1987; Christensen, 1996). The 410-km discontinuity accelerates a slab subduction (e.g., Solheim and Peltier, 1994a; Tackley et al., 1994) while the 660-km discontinuity blocks the slab into the lower mantle (e.g., Christensen and Yuen, 1984, 1985; Fukao et al., 1992; Ita and King, 1994; Bina and Helffrich, 1994; Ito and Yamada, 1982; Čížková and Bina, 2013). If a low ratio of subducting slab-to-mantle viscosity exists, shorter plates promote trench advance and slab rollover geometries, whereas longer plates produce continuous trench retreat and backward slab draping geometries. Conversely, for a high ratio of subducting slab-to-mantle viscosity, the opposite occurs (Xue et al., 2020). However, these models primarily simulate the free subduction of a slab without considering the slab's subduction history, making it challenging to provide in-depth insights into the dynamics of a specific slab subduction.

The Pacific plate is very special. It has lain in the MTZ and moved westward a considerable distance, exceeding 1200 km from the Japan Trench beneath the CVP, as evidenced by seismic tomography studies (e.g., Li et al., 2008; Li and van der Hilst, 2010; Wei et al., 2012; Tao et al., 2018; Lu et al., 2019). Therefore, in order to provide a reference for selecting geodynamic model parameters that are used to reproduce the subduction process of the Pacific plate, in this paper, we initially construct a series of 3D thermochemical geodynamic models that assimilate the time-dependent data from the plate reconstruction model of Müller et al. (2016). Then, we simulate the effects of several parameters on the Pacific slab subduction dynamics, focusing particularly on the westward movement distance, sinking depth and structure of the Pacific slab, as well as whether the DCL can be predicted. Finally, we propose guidelines for selecting these parameters to reasonably reproduce the seismic observations beneath the CVP.

2. High-speed anomaly zone beneath the CVP

Seismic tomography has been considered the most important and widely used method for mapping a slab within the mantle. In general, the slab is colder and denser than the surrounding mantle, and therefore exhibits a high seismic velocity anomaly. This anomaly serves as the most important basis for determining the morphology of the slab. Ideally, seismic tomography could map a slab in the mantle completely and precisely. However, in practice, it is difficult to achieve this successfully due to the non-uniform distribution of seismic stations and hypocenters, the heterogeneity of the Earth's interior, the depth-dependent sensitivity of seismic phases, and the resolution limitations of seismic imaging methods. We have collected 22 seismic models, which cover both the Japan subduction zone and Northeast Asia, published over the last 15 years. These models include the FWEA18 P and S (Tao et al., 2018), GAP_P4 (Obayashi et al., 2013; Fukao and Obayashi, 2013), GYPSUM P and S (Simmons et al., 2010), MIT08 (Li et al., 2008; Li and van der Hilst, 2010), LLNL_G3Dv3_Vp (Simmons et al., 2012), TX2019slab P and S (Lu et al., 2019), S40RTS (Ritsema et al., 2011), Savani (Auer et al., 2014), SEMUCB_WM1 (French and Romanowicz, 2014), SEMum (Lekić and Romanowicz, 2011), smean2 (Jackson et al., 2017), IVAN2011 P and S (Koulakov, 2011), Weiwei2012 (Wei et al., 2012), 3D2018-08Sv (Debayle et al., 2016), S2_9EA (Kustowski et al., 2008), HMSLS06 Pand S (Houser et al., 2008), SAW642ANB (Panning et al., 2010), and SEISGLOB2 (Durand et al., 2017). It is found that, among these models, TX2019slab, Weiwei2012, GAP_P4, FWEA18, LLNL_G3Dv3_Vp and MIT08 map the Pacific slab clearer. When examining the three latitude profiles across the CVP for each model (Figs. S1–S3), they all exhibit very similar high-speed anomaly zones located within the MTZ beneath the CVP, suggesting slight variations in the high-speed structure from south to north. If the westernmost position of the high-speed anomaly zone, as marked by the green dash line in Fig. S1, is considered as that of the Pacific slab, it reveals that the Pacific slab has very close westernmost positions in the three latitude profiles for each seismic model, with the exception of TX2019slab P model (Figs. S1a–S3a). Among these models, the maximum difference among the westernmost positions inferred from the three profiles of each model is ~60 km, observed in the TX2019slab S model. Relative to the westernmost position, the differences among the bottom depths are greater. The largest difference in bottom depths is larger than 100 km, observed in both the TX2019slab S and FWEA18 P models (Figs. S1–S3; Table S1). The westernmost positions revealed by the global models of TX2019slab and LLNL_G3Dv3_Vp are significantly closer to the west compared to those indicated by regional models, with the maximum difference exceeding 800 km for the Weiwei2012 and TX2019slab S models. This may stem from differences in the horizontal resolutions of these models.

For instance, the Weiwei2012 model boasts a resolution of ~1.2° (Wei et al., 2012), while the TX2019slab S model has a resolution of ~5° (Lu et al., 2019). Furthermore, the TX2019slab and LLNL_G3Dv3_Vp models also exhibit westernmost positions that are significantly further to the west compared to the global models of MIT_08 and GAP_P4, with the maximum difference exceeding 600 km for the MIT_08 and TX2019slab S models. Because of the close horizontal resolutions of ~5° for TX2019slab, LLNL_G3Dv3_Vp and MIT08, the reason for this significant difference remains unclear. Notably, there is a noticeable difference in the westernmost positions between the regional models of Weiwei2012 and FWEA18, with the maximum difference exceeding 200 km, despite the fact that they have comparable resolutions (Weiwei2012: 1.2; FWEA18: 50–80 km) (Figs. S1–S3; Table S1).

It is surprising that there are significant differences among the westernmost positions of the Pacific slab mapped by these seismic models, even though they have comparable horizontal resolutions. Accordingly, we do not think that it is reasonable for taking the westernmost position of the high-speed anomaly zone in the MTZ as that of the subducting Pacific slab. Actually, the regional models with much higher resolutions, especially FWEA18, show that the notable velocity difference is between the west and the east at a longitude of ~120°E (Cyan line; Figs. S1c, S1e, S1f). Therefore, we believe that the eastern side is attributed to the Pacific slab, while the western side is likely caused by other mechanisms such as the delamination of continental lithosphere. MIT08 is a global model with a horizontal resolution of ~5°, yet it maps the Pacific slab very clearly, comparable to Weiwei2012 and FWEA18. These models (MIT08, Weiwei2012 and FWEA18) indicate that the westernmost positions of the Pacific slab are situated at 120.07°E - 120.75°E (Figs. S1c, e, f, h), 120.01°E - 120.90°E (Figs. S2c, e, f, h), and 119.94°E - 121.59°E (Figs. S3c, e, f, h) across the three latitude profiles, with differences of approximately 55 km, 75 km and 135 km, respectively, which are comparable to their horizontal resolutions. Furthermore, the bottom depths of the Pacific slab are located at 660–740 km, 660–750 km, and 660–740 km, with differences of less than 100 km (Table S2). In this study, we take the arithmetic mean of the velocity anomalies from the three models as the observable shown as Fig. 2 whose position is located at latitude 41.67°E, as indicated in Fig. 1. The observable indicates that the high-speed anomaly zone in the MTZ beneath the CVP is caused by two distinct components. One is the Pacific slab, which lies within the MTZ with its westernmost position at approximately 120°E and a bottom depth that is mostly shallower than 800 km. The other component, named DCL in this paper, connects with the westernmost end of the Pacific slab and extends westward towards approximately 114°E. The latter is likely related to the detachment of continental lithosphere. Additionally, the global models of TX2019slab, MIT08, and GAP_P4 reveal that the Izanagi slab does not make contact with but instead lies beneath the high-speed anomaly zone (Fig. S4).

3. Model setup

In order to explore the effects of several parameters on the dynamics of Pacific plate subduction, we have established 3D thermochemical geodynamic models using data assimilation technique (Hu et al., 2016, 2017; Peng et al., 2021a, 2021b) to simulate the subduction history of the Pacific plate since the Cenozoic. The mantle is assumed to be incompressible and follows the Boussinesq approximation, whereby the thermochemical mantle convection is governed by the equations for the conservation of mass, momentum and energy and the advection of chemical particles.

$$\nabla \bullet \vec{u} = 0, \tag{1}$$

$$-\nabla P + \nabla \bullet \left[\eta\left(\nabla \vec{u} + \nabla^T \vec{u}\right)\right] + \left(\rho_m \alpha \Delta T + \Delta\rho_c\right)\vec{g} = 0, \tag{2}$$

$$\frac{\partial T}{\partial t} + \vec{u} \bullet \nabla T = \kappa \nabla^2 T, \tag{3}$$

$$\frac{\partial C}{\partial t} + \vec{u} \bullet \nabla C = 0, \tag{4}$$

where $\vec{u}$ is the velocity, P is the dynamic pressure, η is the dynamic viscosity, ρ_m is the density of the ambient mantle, α is the thermal expansion coefficient, ΔT is the temperature anomaly, $\Delta\rho_c$ is the compositional density anomaly, $\vec{g}$ is the gravitational acceleration, and C is the composition.

The CVP is located ~127–129°E and ~ 41.33–42.67°N (Fig. 1). Our study area is a very small region, covering only a range of ~2° and ~ 1.5° in longitude and latitude, respectively. However, the model domain is set to be sufficiently wide, with the nearest vertical boundary being >2000 km away from any part of the study area, in order to avoid artificial return flow from side walls (e.g., Liu and Stegman, 2011; Zhu, 2014). The model is discretized with 865 × 193 × 161 nodes in longitude, latitude and depth, respectively. The mesh resolution is ~46 km in latitude, ~4–22 km in longitude and ~ 16 km near and within the CVP. The depth resolution is ~7 km near the surface, 10 km between 20 km and 710 km, gradually increasing to ~35 km at a depth of ~1800 km, and remaining at this resolution until the core-mantle boundary. We utilize the 3D spherical finite element code CitcomS (Moresi et al., 1996; Zhong et al., 2000, 2008; Tan et al., 2006) to simulate Pacific slab subduction and mantle convection by solving the governing equations. The basic model parameters are listed in Table 1.

The past plate motion and seafloor age (Fig. 3), derived from the plate reconstruction by Müller et al. (2016), are used to update the surface velocity boundary condition and the upper thermal boundary layer, respectively, at every time step. All other boundaries are free slip. The core-mantle boundary has a fixed temperature, which is set at 2500 °C, a realistic value near the boundary (e.g., Steinberger and Calderwood, 2006; Mao and Zhong, 2018). The open source software GPlates (www.gplates.org; Gurnis et al., 2012) is utilized to reconstruct the surface velocity and seafloor age over an interval of 1 *Ma*. At any given time within this interval, they are interpolated linearly.

The temperature structure of oceanic plates satisfies the half-space cooling model (Turcotte and Schubert, 2014) and is updated by assimilating the seafloor age at each time step. Continental lithospheric temperature is assumed to obey the plate cooling model (Turcotte and

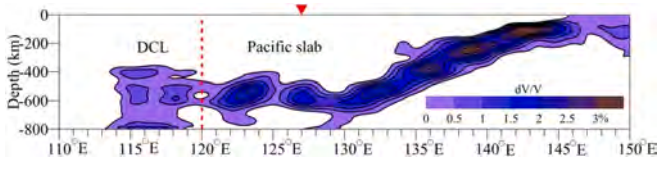

Fig. 2. Seismically inferred high-speed anomaly zone beneath the Changbaishan volcanic province (red triangle) used in this study. (For interpretation of the references to colour in this figure legend, the reader is referred to the web version of this article.)

Table 1
Model parameters.

Parameter	Value
Earth's radius, R	6371 km
Mantle thickness, h	2867 km
Mantle density, ρ_m	3340 kg/m^3
Gravitational acceleration, g	9.8 m/s^2
Thermal diffusivity, κ	10^{-6} m^2/s
Thermal expansivity, α	3×10^{-5} K^{-1}
Mantle temperature, T_m	1300 °C
Temperature difference across mantle	2500 °C
Reference viscosity, η_0	10^{21} Pa·s
Rayleigh number, Ra	6.35×10^8
Maximum viscosity cutoff, η_{max}	10^{24} Pa·s
Minimum viscosity cutoff, η_{min}	10^{18} Pa·s

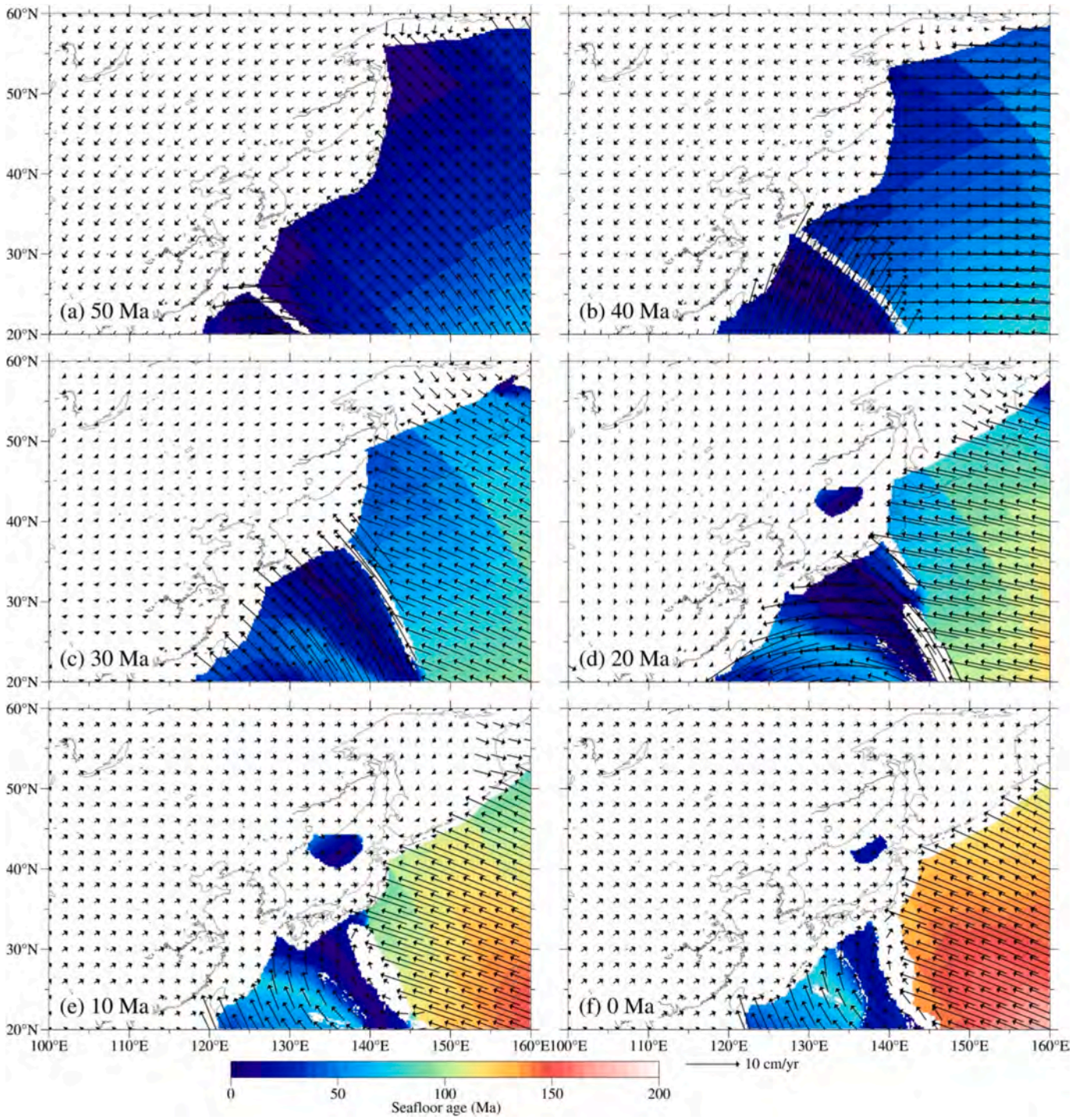

Fig. 3. Plate motions and seafloor age since 50 *Ma* inferred from the plate reconstruction of Müller et al. (2016).

Schubert, 2014). The lithospheric thickness is set to 100 km, which is comparable to that of Northeast China (An and Shi, 2006), and the bottom lithospheric temperature is set to the mantle temperature of 1300 °C (e.g., Kumar and Gordon, 2009; Jiménez-Díaz et al., 2012).

Different chemical compositions are considered in our thermo-chemical geodynamic models. The compositional density anomaly is calculated using the ratio method (e.g., Hu et al., 2016, 2017, 2018; Peng et al., 2021a, 2021b).

$$B = \frac{\Delta\rho_c}{\alpha_0 \rho_0 \Delta T}, \tag{5}$$

where B is the buoyancy ratio, an input parameter that varies with different compositions, $\Delta\rho_c$ the compositional density anomaly, ρ_0 the reference density, α_0 the reference thermal expansivity, and ΔT the temperature contrast across the mantle.

The continental lithosphere is composed of a ~ 20-km thick upper crust, a ~ 15-km thick lower crust and a ~ 65-km thick mantle lithosphere (Fig. S5). According to the ak135 (Kennett et al., 1995) or iasp91 (Kennett and Engdahl, 1991) models, the average density of the upper crust is ~2.72 g/cm^3, and that of the lower crust is ~2.92 g/cm^3, indicating an average density of continental crust of ~2.82 g/cm^3; the mantle lithosphere is a chemically buoyant layer with a density of

~3.33 g/cm^3, which results in an almost purely thermal mantle lithosphere. The oceanic plate consists of a ~ 7-km thick weak oceanic crust and a ~ 20-km thick chemically buoyant layer that mimics a basaltic crust (Fig. S5). The weak crust, which is neutrally buoyant, exhibits high viscosity far away from a trench (> ~300 km) but a low viscosity of 10^{19} Pa·s near the trench (≤ ~300 km), thus acting as a lubricating layer to decouple a subducting plate from an overriding plate (e.g., Hu et al., 2016, 2017, 2018; Peng et al., 2021a, 2021b). This weak crustal layer serves a similar function of a sticky air layer, which is crucial for producing asymmetric subduction and realistic topography (Crameri et al., 2012). The buoyant crustal layer lies beneath the weak oceanic crust and has a total buoyancy equivalent to that of a 7-km thick basalt crust with a density of 3.0 g/cm^3. When the chemically buoyant oceanic crust is subducted to 120 km or deeper, its composition changes to eclogite following the basalt-to-eclogite phase transformation, and consequently, its total buoyancy becomes equivalent to that of a 7-km thick eclogite layer with a density of 3.68 g/cm^3. When a new subduction zone forms, an arc-like weak zone is created on the overriding side (Hu et al., 2018). Therefore, following previous investigators (e.g., Hu et al., 2016, 2017, 2018; Peng et al., 2021a, 2021b), we arrange an arc-like weak zone positioned between the continental and oceanic plates to mimic the properties of Earth's subduction zones. This zone is charactered by a viscosity of 10^{19} Pa·s, a density of 2.92 g/cm^3, a thickness of ~40-km, and a length ranging from 300 km (top side) to 350 km (bottom side) (Fig. S5). It aids in decoupling the subducting oceanic plate from the overriding continental plate on both sides of the subduction zone during the subduction process.

The 3D viscosity used varies with depth, temperature and composition (e.g., Hu et al., 2018; Peng et al., 2021a, 2021b) following

$$\eta = \eta_0 \bullet C \bullet exp\left(\frac{E_\eta}{T + T_\eta} - \frac{E_\eta}{T_m + T_\eta}\right), \quad (6)$$

where η is the effective viscosity, η_0 is the depth-dependent background viscosity, C is the compositional multiplier, E_η is the activation energy, T_η is the temperature offset, T is the temperature and T_m is the mantle temperature. The background viscosity η_0, activation energy E_η and activation temperature T_η vary within four different depth ranges of 0–100 km, 100–300 km, 300–660 km and 660–2867 km. For a reference model, the background viscosity of these layers is 10^{20} Pa.s, 10^{20} Pa.s, 10^{21} Pa.s (η_{mtz}) and 3 × 10^{22} Pa.s (η_{lw}), respectively. The activation energy E_η is 25, 42, 25 and 17 kJ/mol, respectively, for the four layers. The temperature offset T_η of these layers is 100, 100, 300 and 300 °C, respectively. Composition affects viscosity by introducing a multiplier C, which is a geometric average for all the compositions within an element, to the pre-exponential factor of viscosity (e.g., Hu et al., 2018; Peng et al., 2021b).

The initial temperature and viscosity are the outputs of Model 1, a reference model presented by Peng et al. (2021a), at 50 *Ma*. Model 1 of Peng et al. (2021a) was a 3D global thermochemical model incorporating data assimilation and ran from 200 *Ma*, under the constraints of plate motion history and seafloor age reconstructed by Müller et al. (2016). In other words, Model 1 reconstructed the global subducting slabs and mantle structures since 200 Ma. There are two primary reasons why we utilize the outputs of Model 1 from Peng et al. (2021a). Firstly, our regional models, regardless of starting at 200 *Ma*, 150 *Ma*, or 120 *Ma*, are unable to reproduce the Izanagi slab, which significantly affects the Pacific plate subduction dynamics and the formation of stagnant slabs within the MTZ (Peng et al., 2021a). Secondly, the structures produced by Model 1 are similar to those derived from seismic tomography on a large scale, but it remains challenging to delve into regional-scale issues in-depthly. Furthermore, the stagnant slab within the MTZ originates from the Pacific plate, which likely starts to subduct at 20–30 *Ma* (Mao and Zhong, 2018), beneath the CVP, thus our goal can be achieved by running geodynamic models since 50 *Ma*.

4. Results

As mentioned above, our primary focus is on the impacts of several parameters on the westward movement distance, sinking depth, and structure of the Pacific slab. Additionally, we examine whether geodynamic models incorporating these parameters can well predict both the Pacific slab and the DCL within the modern mantle. Consequently, we provide a brief overview of previous studies and present our detailed modeling results herein.

4.1. Effects of uppermantle seismic discontinuities

There are two main global seismic discontinuities in the upper mantle: the 410-km and 660-km discontinuities, which have been considered as phase transition boundaries (e.g., Collier et al., 2001; Ringwood, 1969). The 410-km discontinuity represents the exothermic boundary of the α-olivine to β-spinel transition, featuring a positive Clapeyron slope. Consequently, negative buoyancy is generated and attaches to a subducting slab near this discontinuity, accelerating the slab's subduction into the MTZ and slightly enhancing the transportation of upper mantle materials and the penetration of the slab through the 660-km discontinuity (Solheim and Peltier, 1994b; Tackley et al., 1994). However, some investigators hold opposing views regarding the effects of the olivine-spinel transition on the penetration of the 660-km discontinuity (e.g., Zhao et al., 1992; Steinbach and Yuen, 1992). The Clapeyron slope (γ_{410}) and thickness (δh_{410}) of the 410-km discontinuity range from 1.0 to 3.8 MPa/K (Akaogi et al., 1989, 2007; Katsura and Ito, 1989; Chopelas, 1991; Bina and Helffrich, 1994; Morishima et al., 1994; Lebedev et al., 2002) and from 2 to 40 km (Akaogi et al., 1989; Katsura and Ito, 1989; Petersen et al., 1993; Yamazaki and Hirahara, 1994; Xu et al., 2003; Tibi and Wiens, 2005; Zou, 2018; Li et al., 2019b, 2022; Vinnik et al., 2020). The 660-km discontinuity is the endothermic boundary of the transition from ringwoodite to bridgmanite and magnesiowüstite. This boundary, generally speaking, has a negative Clapeyron slope. Consequently, positive buoyancy is generated and attaches to a subducting slab near the discontinuity, hindering the slab's sinking into the lower mantle. Some investigators have considered this to be the primary cause of stagnant slabs in the MTZ (e.g., Christensen and Yuen, 1984, 1985; Fukao et al., 1992; Ita and King, 1994; Bina and Helffrich, 1994; Ito and Yamada, 1982; Čížková and Bina, 2013), while others do not believe that the buoyancy resulting from the phase transition at this boundary is sufficient to compensate for the density of a cold subducting slab (e.g., Christensen, 1996; Ita and King, 1998; Fukao et al., 2009; King, 2007; Yanagisawa and Yamagishi, 2005). The Clapeyron slope (γ_{660}) and thickness (δh_{660}) of the 660-km discontinuity range from −0.4 to −6 MPa/K (Ito and Yamada, 1982; Ito and Takahashi, 1989; Ito et al., 1990; Akaogi and Ito, 1993; Chopelas et al., 1994; Bina and Helffrich, 1994; Lebedev et al., 2002; Hirose, 2002; Katsura et al., 2003; Fei et al., 2004; Litasov et al., 2005a, 2005b; Akaogi et al., 2007; Ghosh et al., 2013; Kojitani et al., 2016) and from ~2 km to ~70 km (Wang and He, 2020; Zhang et al., 2019; Li et al., 2013; Wang and Niu, 2010; Tibi and Wiens, 2005; Xu et al., 2003; Castle and Creager, 2000; Yamazaki and Hirahara, 1994; Benz and Vidale, 1993; Petersen et al., 1993; Revenaugh and Jordan, 1991). The δh_{660} is between ~35 and 70 km in Northeast China (Li et al., 2013; Ye et al., 2011; Wang and Niu, 2010). These results indicate that the two discontinuities have the wide ranges of the Clapeyron slopes and thicknesses. In general, the smaller the γ_{410}, the smaller the force attaching to a subducting slab near the 410-km discontinuity, resulting in a smaller acceleration of the slab. Consequently, the slab penetrates the 660-km discontinuity into the lower mantle to a lesser extent (Čížková and Bina, 2013; Kincaid and Olson, 1987); the smaller the $|\gamma_{660}|$, the easier the slab penetrates the 660-km discontinuity, and the deeper the slab sinks into the lower mantle. It favors predicting a stagnant slab in the MTZ mapped by seismic tomography, using a geodynamic model that incorporates a γ_{660} ranging from −1.5 to −8 MPa/K (−1.5 to −3.0 MPa/

K, Ma et al., 2019; −2.0 MPa/K, Mao and Zhong, 2018; −4.0 MPa/K, Tackley et al., 1993; −6 to −8 MPa/K, Christensen and Yuen, 1984, 1985; −5 to −6 MPa/K, Ita and King, 1994; −3 to −6 MPa/K, King and Ita, 1995; −2.8 to −5.6 MPa/K, Christensen, 1996; -4 MPa/K, Davies, 1995; −−4 MPa/K, Zhong and Gurnis, 1994), without considerating the 410-km discontinuity, while when considering the 410-km discontinuity, the γ_{410} generally takes 3 to 4 MPa/K and the γ_{660}–2 to −6 MPa/K (Peng et al., 2021a; Yang et al., 2018; King et al., 2015). It may well reproduce the stagnant Pacific slab in the MTZ beneath East Asia using geodynamic models that consider either $\gamma_{660} = -1.5$ to −3 MPa/K and $\delta h_{660} = 40$ km (Ma et al., 2019) or $\gamma_{660} = -2$ MPa/K and $\delta h_{660} = 40$ km (Mao and Zhong, 2018) in the absence of the 410-km discontinuity. Alternatively, when considering the 410-km discontinuity, it may use models with either $\gamma_{410} = 4$ MPa/K, $\gamma_{660} = -2$ MPa/K and $\delta h_{410} = \delta h_{660} = 64$ km (Peng et al., 2021a) or $\gamma_{410} = 3$ MPa/K and $\gamma_{660} = -3$ MPa/K (Yang et al., 2018) in the presence of the 410-km discontinuity. These studies have provided us with basic knowledge of the effects of the two discontinuities on slab subduction dynamics, but in the meantime, we find that previous workers (e.g., Christensen and Yuen, 1984, 1985; Čížková and Bina, 2013; Peng et al., 2021a; Yang et al., 2018; King et al., 2015; Ma et al., 2019; Mao and Zhong, 2018) have presented a wider range of Clapeyron slopes and thicknesses for the 410-km and 660-km discontinuities, aiming to replicate the stagnant slab structure in the MTZ. Consequently, it is essential to clarify the impacts of these two discontinuities on the dynamic process of Pacific plate subduction, as well as the slab structure, westward movement distance, and sinking depth within the mantle. We (Zhu et al., 2024) conducted this work using the models M1 – M24 listed in Table 2 and submitted the results to a Chinese journal. Here, we briefly summarize the key findings. The westernmost positions and bottom depths of the Pacific slab predicted by the models M1 – M24 that incorporate varying values of γ_{410}, γ_{660}, δh_{410} and δh_{660}, are plotted in Fig. 4a–e. We found that (1) the γ_{410}, to a certain degree, affects the westward movement distance of the Pacific slab in the mantle, while it slightly influences the sinking depth of the slab. As the γ_{410} decreases, the average movement distance increases gradually, and the sinking depth becomes slightly shallower. The maximum differences are ~80 km and ~ 50 km for the distance and sinking depth, respectively, over a range of γ_{410} from 0 to 6 MPa/K; (2) with the increase of $|\gamma_{660}|$, the effect of γ_{410} gradually weakens. When $|\gamma_{660}| \geq 4$ MPa/K, the effect of γ_{410} can be almost ignored; (3) the γ_{660} has significant effects on both the westward movement distance and sinking depth of the Pacific slab in the mantle. When $|\gamma_{660}| \leq 5$ MPa/K, the average slab westward movement distance increases as $|\gamma_{660}|$ increases. However, when $|\gamma_{660}| > 5$ MPa/K, the situation reverses; that is, the larger the $|\gamma_{660}|$, the smaller the average slab westward movement distance. The sinking depth consistently becomes shallower with the increase of $|\gamma_{660}|$. The maximum differences exceed 300 km and 600 km for the distance and sinking depth, respectively, over a range of γ_{660} from −1 MPa/K to −6 MPa/K; (4) both δh_{410} and δh_{660} have slight effects on the dynamic processes of the Pacific slab and the slab structure within the mantle; (5) a geodynamic model that merely considers the effects of both 410-km and 660-km discontinuities may predict the westernmost position of the Pacific slab in the modern mantle reasonably, but it struggles to reproduce the slab's sinking depth reasonably and the DCL shown in Fig. 2.

4.2. Effects of the lower mantle viscosity

The viscosity jump (η_{lw}) across the 660-km discontinuity, that is, the ratio of the lower mantle viscosity to the upper mantle viscosity, significantly affects the behavior of a slab's penetration through the 660-km discontinuity. In general, a slab's subduction velocity decreases near the 660-km discontinuity as the viscosity jump increases, which makes it increasingly difficult for the slab to penetrate the discontinuity. Therefore, an increase in viscosity in the lower mantle favors the stagnation of the slab in the MTZ (e.g., Čížková and Bina, 2013; Funiciello et al., 2004; Kincaid and Olson, 1987; Christensen and Yuen, 1985; Crameri and Lithgow-Bertelloni, 2018). However, what is a reasonable value for the viscosity jump? This problem has not yet been solved until now. Different values have been proposed using various methods and datasets. The jump has been estimated to be 10–316 for interpreting the geoid anomalies (Hager, 1984; Hager et al., 1985; Hager and Richards, 1989; King and Masters, 1992; Ricard et al., 1993; Liu and Zhong, 2016; Liu et al., 2021), 1–100 for interpreting the variations in post-glacial sea-level (Cathles, 1975; Nakada and Lambeck, 1989; Tushingham and Peltier, 1992; Mitrovica and Peltier, 1993, 1995), 30–250 inferred from the inversion of convection-related observables (free-air gravity harmonics, the excess ellipticity of the CMB and horizontal divergence components of plate motions) (Forte and Mitrovica, 2001), and 2–250 inferred from joint inversion of geoid/free-air gravity anomalies and post-glacial relative sea-level variations (Wu and Peltier, 1983; Forte and Mitrovica, 1996; Mitrovica and Forte, 1997; Paulson et al., 2007). Some researchers have inferred that the viscosity does not jump significantly across the 660-km discontinuity but rather displays high viscosity in the middle of the lower mantle. The high viscosity zone is estimated to be ~40–210 times the viscosity just below the discontinuity, as inferred from a joint inversion of convection-related observables and glacial isostatic adjustment (Mitrovica and Forte, 2004), and ~ 35–80 times the viscosity of the MTZ, as inferred from a joint inversion of whole-mantle P-wave velocity, S-wave velocity, and density variations (Rudolph et al., 2020). A more complex relationship may exist between the viscosities above and below the 660-km discontinuity. The viscosity may increase significantly, decrease significantly, or remain nearly unchanged (Kido et al., 1998). These results present a very wide range of possible viscosity jumps, making it difficult for us to choose a reasonable value to well reproduce the Pacific slab beneath the CVP. Therefore, it is necessary to further study the effects of lower mantle viscosity.

We set the viscosity jump η_{lw} = 30, 50, 100, 150 and 200, corresponding to the models M25 – M29 listed in Table 2, for exploring its effects. It is noted that the temperature deviation (δT) is relative to the mantle temperature T_m, and we commonly use the −50 °C isotherm to determine both the westernmost position and bottom depth in this study, unless specially mentioned. Since the −50 °C isotherm is not distinguishable for $\eta_{lw} \geq 100$ (Fig. 5), the −250 °C isotherm is used in this section. The predicted bottom depths of the Pacific slab (estimated based on the −250 °C isotherm) are 1055, 980, 900, 860 and 820 km for η_{lw} = 30, 50, 100, 150 and 200, respectively (Figs. 4f and 5). This indicates that the sinking depth of the Pacific slab gradually becomes shallower with increasing viscosity jump, consistent with previous studies (Čížková and Bina, 2013; Crameri and Lithgow-Bertelloni, 2018), as expected. However, the westernmost positions are 123.58°E (M25), 125.48°E (M26), 127.27°E (M27), 126.81°E (M28) and 126.48°E (M29) (Figs. 4f and 5), indicating that the westward movement distance of the Pacific slab, with the increase of η_{lw}, decreases initially and then increases. Among these, the maximum distance is found at $\eta_{lw} = 30$. These results reveal that an increase in the lower mantle viscosity could cause a more stagnant Pacific slab in the MTZ, but at the same time, shorten its westward movement distance in the mantle.

The dynamic process beginning at 40 *Ma* (Fig. 6) shows that an increase in η_{lw} leads to a decrease in both the mantle flow velocity and the Pacific slab subduction velocity. The former primarily results in a reduction in the sinking and westward movement velocities of the Izanagi slab, while the latter affects the Pacific slab. However, the decrease in the Pacific slab subduction velocity slows down its westward movement in the mantle, but it still moves significantly faster than the Izanagi slab. Consequently, there is spatial overlap between the western end of the Pacific slab and the eastern end of the Izanagi slab. For a small η_{lw} (e.g., ≤ 50), the Izanagi slab sinks faster. When the westernmost end of the Pacific slab arrives at the easternmost position of the Izanagi slab, the latter has already sunk below the former, therefore, the Izanagi slab does not hinder the westward movement of the Pacific slab. However, since

Table 2
Geodynamic model parameters.

Model	410 km		660 km			η_{lw}	B_6	t_o	η_{mtz}	η_{mlw}	$\Delta\rho_{asth}$ %
	γ_{410} MPa/K	δh_{410} km	γ_{660} MPa/K	δh_{660} km	$\Delta\rho_{660}$%						
Effects of γ_{410} (Zhu et al., 2024)											
M1	0	20	-2	20	8	30	−0.48	1	1	30	0
M2	1	20	−2	20	8	30	−0.48	1	1	30	0
M3	2	20	−2	20	8	30	−0.48	1	1	30	0
M4	3	20	−2	20	8	30	−0.48	1	1	30	0
M5	4	20	−2	20	8	30	−0.48	1	1	30	0
M6	5	20	−2	20	8	30	−0.48	1	1	30	0
M7	6	20	−2	20	8	30	−0.48	1	1	30	0
M8	0	20	−6	20	8	30	−0.48	1	1	30	0
M9	1	20	−6	20	8	30	−0.48	1	1	30	0
M10	2	20	−6	20	8	30	−0.48	1	1	30	0
M11	3	20	−6	20	8	30	−0.48	1	1	30	0
M12	4	20	−6	20	8	30	−0.48	1	1	30	0
M13	5	20	−6	20	8	30	−0.48	1	1	30	0
M14	6	20	−6	20	8	30	−0.48	1	1	30	0
Effects of δh_{410} (Zhu et al., 2024)											
M15	2	40	−2	20	8	30	−0.48	1	1	30	0
M16	2	60	−2	20	8	30	−0.48	1	1	30	0
Effects of γ_{660} (Zhu et al., 2024)											
M17	2	20	−1	20	8	30	−0.48	1	1	30	0
M18	2	20	−3	20	8	30	−0.48	1	1	30	0
M19	2	20	−4	20	8	30	−0.48	1	1	30	0
M20	2	20	−5	20	8	30	−0.48	1	1	30	0
Effects of δh_{660} (Zhu et al., 2024)											
M21	2	20	−2	40	8	30	−0.48	1	1	30	0
M22	2	20	−2	60	8	30	−0.48	1	1	30	0
M23	2	20	−2	80	8	30	−0.48	1	1	30	0
M24	2	20	−2	100	8	30	−0.48	1	1	30	0
Effects of η_{lw} (this study)											
M25	2	40	−4	40	8	30	−0.48	1	1	30	0
M26	2	40	−4	40	8	50	−0.48	1	1	30	0
M27	2	40	−4	40	8	100	−0.48	1	1	30	0
M28	2	40	−4	40	8	150	−0.48	1	1	30	0
M29	2	40	−4	40	8	200	−0.48	1	1	30	0
Effects of B_6 (this study)											
M30	2	40	−4	40	8	30	0	1	1	30	0
M31	2	40	−4	40	8	30	−0.24	1	1	30	0
M32	2	40	−4	40	8	30	−0.72	1	1	30	0
M33	2	40	−4	40	8	30	−1	1	1	30	0
Effects of t_o (this study)											
M34	2	40	−4	40	8	30	−0.48	0.5	1	30	0
M35	2	40	−4	40	8	30	−0.48	0.75	1	30	0
M36	2	40	−4	40	8	30	−0.48	1.25	1	30	0
M37	2	40	−4	40	8	30	−0.48	1.5	1	30	0
Effects of η_{mtz} (this study)											
M38	2	40	−4	40	8	30	−0.48	1	2.5	30	0
M39	2	40	−4	40	8	30	−0.48	1	5.0	30	0
M40	2	40	−4	40	8	30	−0.48	1	7.5	30	0
M41	2	40	−4	40	8	30	−0.48	1	10.0	30	0
Effects of η_{mlw} (this study)											
M42	2	40	−4	40	8	30	−0.48	1	1	50	0
M43	2	40	−4	40	8	30	−0.48	1	1	100	0
M44	2	40	−4	40	8	30	−0.48	1	1	150	0
Effects of $\Delta\rho_{asth}$ (this study)											
M45	2	40	−4	40	8	30	−0.48	1	1	30	−1
M46	2	40	−4	40	8	30	−0.48	1	1	30	−2
M47	2	40	−4	40	8	30	−0.48	1	1	30	−3

(continued on next page)

Table 2 (*continued*)

Model	410 km		660 km			η_{lw}	B_6	t_o	η_{mtz}	η_{mlw}	$\Delta\rho_{asth}$ %
	γ_{410} MPa/K	δh_{410} km	γ_{660} MPa/K	δh_{660} km	$\Delta\rho_{660}$%						
Effects of $\Delta\rho_{660}$ (this study)											
M48	2	40	−4	40	4	30	−0.48	1	1	30	0
M49	2	40	−4	40	10	30	−0.48	1	1	30	0
M50	2	40	−4	40	15	30	−0.48	1	1	30	0

Note: η_{mlw} is the non-dimensional viscosity at the 1500–2500 km depth; $\Delta\rho_{asth}$ is the density contrast of oceanic asthenosphere relative to ambient mantle.

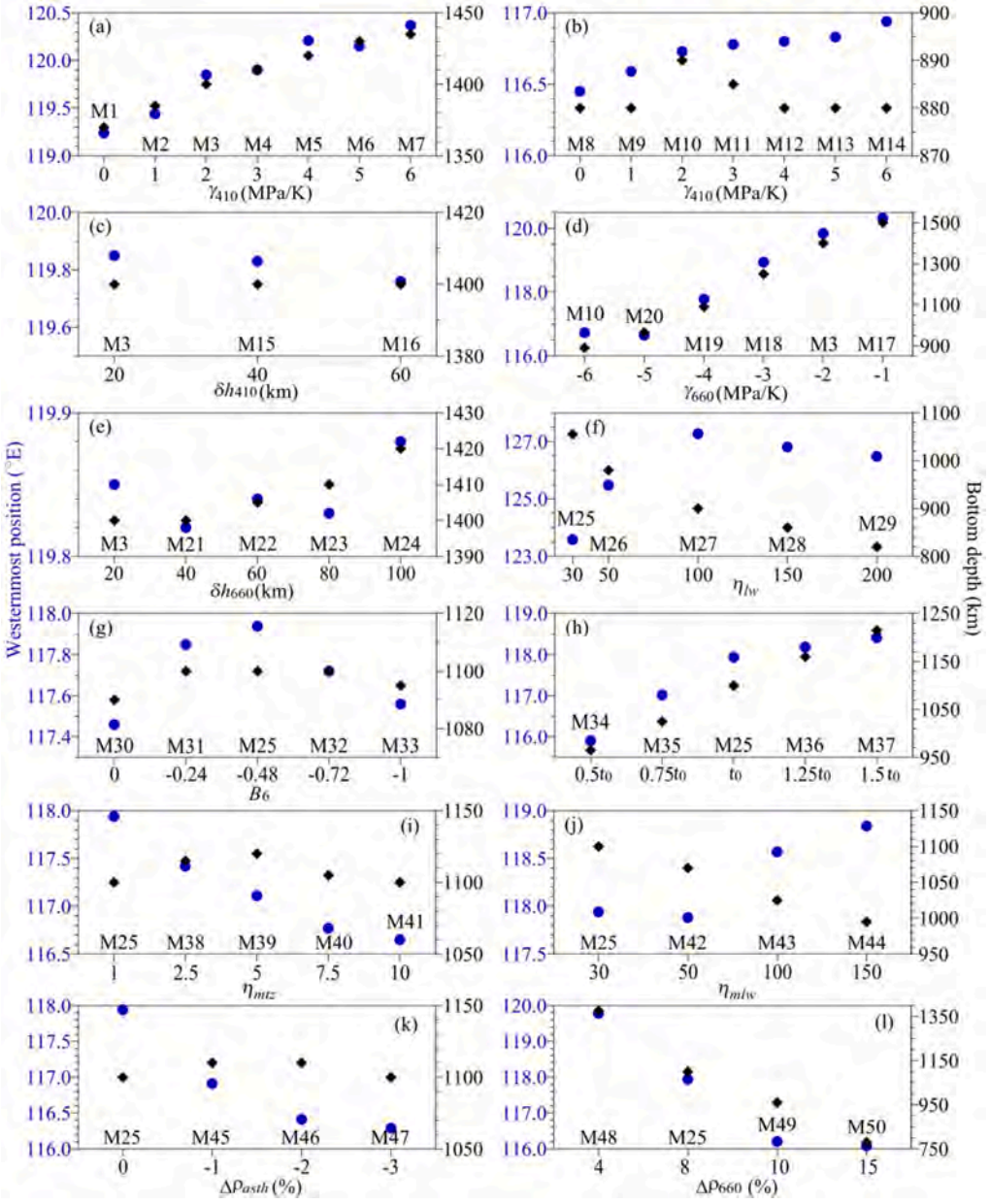

Fig. 4. Westernmost posotions and bottom depths of the Pacific slab predicted by geodynamic models M1 – M50 listed in Table 2. The positions and depths for models M25 to M29, shown in (f), are determined based on the −250 °C isotherm, while those for the other models are determined based on the −50 °C isotherm.

an increase in η_{lw} decreases the velocity of horizontal mantle flow and Pacific slab subduction, the model with a larger η_{lw} (e.g., 50) predicts a shorter westward movement distance of the Pacific slab compared to the model with a smaller η_{lw} (e.g., 30) (Figs. 5 and 6). In addition, as η_{lw} increases, the continental lithosphere delamination gradually intensifies, but the delaminated material does not adhere to the westernmost end of the Pacific slab (Fig. 6). For a large η_{lw} (e.g., $\geq$ 100), the Izanagi slab sinks more slowly. When the westernmost end of the Pacific slab arrives at the easternmost position of the Izanagi slab, the latter has not fully sunk below the former, resulting in contact between the two slabs. Consequently, the Izanagi slab impedes the westward movement of the Pacific slab (Fig. 7). The impeding effect of the Izanagi slab, combined with the decrease in horizontal mantle flow velocity and the Pacific slab subduction velocity due to the increased η_{lw}, leads to a

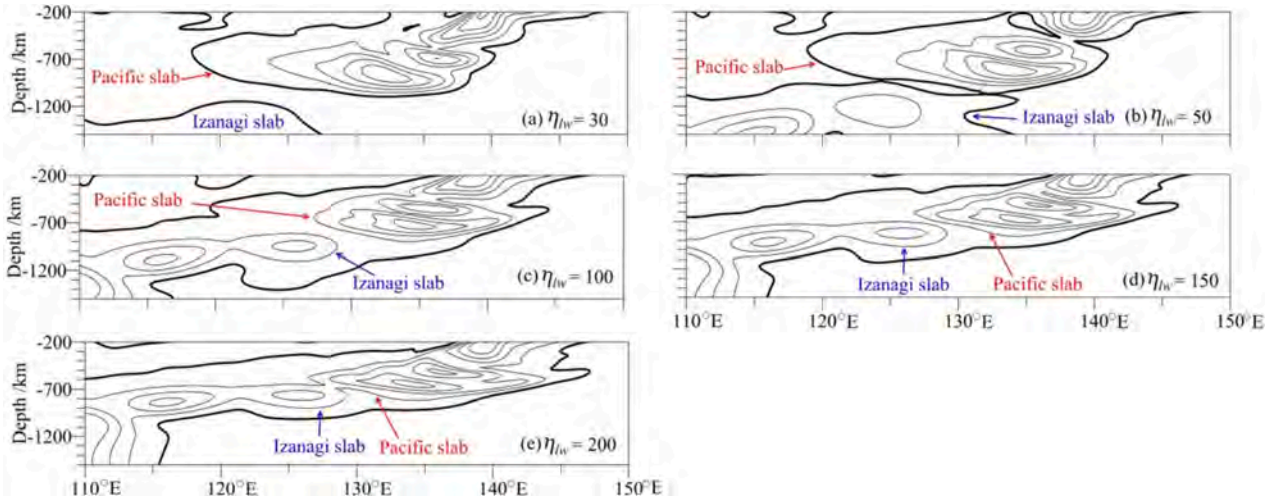

Fig. 5. Present-day (0 *Ma*) Pacific slab structure in the mantle predicted by the models M25 - M29. The thick line stands for the isotherm where temperature deviation (δT) relative to the mantle temperature (T_m) is equal to −250 °C. The isotherm interval is 200 degrees Celsius. The temperature.

significant shortening of the westward movement distance of the Pacific slab. For instance, the westward movement distance for $\eta_{lw} = 100$ is approximately 300 km shorter than that for $\eta_{lw} = 30$. Furthermore, little delamination occurs in this scenario (Fig. 7).

Seismic tomography has revealed that the westernmost end of the Pacific slab beneath the CVP has arrived at ~120°E, and its bottom depth is almost shallower than 800 km (Table S2; Fig. 2). The models M25 ($\eta_{lw} = 30$) and M26 ($\eta_{lw} = 50$) predict the westernmost positions at 117.94°E and 118.87°E, and the bottom depths at 1100 km and 1065 km, respectively. This suggests that the two models may reproduce the westernmost position well, but they are unable to reasonably predict the bottom depth of the Pacific slab beneath the CVP. In addition, none of the models with varying η_{lw} predict the DCL, with the westernmost position at ~114°E (Fig. 2), on the west of the Pacific slab. These findings suggest that a geodynamic model solely considering the viscosity jump η_{lw} may predict well the westernmost position of the Pacific slab in the modern mantle, but it struggles to reproduce the slab sinking depth and the DCL revealed by seismic tomography.

4.3. Effects of the chemically buoyant layer

As mentioned in Section 3, we incorporate a chemically buoyant layer to mimic a basaltic crust. Specifically, the chemical buoyancy of this layer is equivalent to that of a 7 km-thick Earth's basaltic oceanic crust. It is commonly understood that the average density of Earth's oceanic crust is ~3.0 g/cm^3, but this density can vary widely between 2.7 and 3.1 g/cm^3 (Carlson and Raskin, 1984; Carlson and Herrick, 1990). Therefore, in order to probe the effects of the chemically buoyant layer, we set the buoyancy ratio B_6 is 0 (no chemical buoyancy; M30), −0.24 (M31), −0.48 (M25), −0.72 (M32) and − 1.0 (M33) to mimic the chemical buoyancy due to a 7 km-thick basaltic layer with density of 3.34, 3.17, 3.0, 2.83 and 2.63 g/cm^3.

These models predict a very similar present-day Pacific slab structure beneath the CVP (Fig. 8), with a minimum cross-correlation coefficient of 0.97 (Table S3). The predicted westernmost positions and bottom depths are 117.46°E and 1090 km (M30), 117.85°E and 1100 km (M31), 117.94°E and 1100 km (M25), 117.72°E and 1100 km (M32), and 117.56°E and 1095 km (M33), respectively (Figs. 4g and 8). Initially, as the chemical buoyancy increases (the B_6 becomes more negative), the westernmost position moves eastward, then slightly westward, indicating that the westward movement distance decreases first and then slightly increases, while the bottom depth hardly varies with the chemical buoyancy of the layer. The maximum difference among these predicted distances is ~40 km, between M30 and M25. These results suggest that the chemically buoyant layer has minimal effects on the structure and sinking depth of the Pacific slab but slight effects on its westward movement distance.

All of these models also predict very similar structure, westernmost position and bottom depth of the Pacific slab at the same subduction period (Figs. S6 and S7), indicating that the chemically buoyant layer does not significantly affect the dynamics of the Pacific slab subduction beneath the CVP. The continental lithospheric delamination increases with the enhancement of the chemical buoyancy of the layer (i.e., a more negative B_6). The delaminated lithosphere typically attaches to the top but not the westernmost end of the Pacific slab, so these models cannot predict the DCL, as shown in Fig. 2. Accordingly, B_6 is not a crucial parameter, and the chemical buoyancy of the layer may be disregarded when reproducing the Pacific slab beneath the CVP.

4.4. Effects of slab age

The age of a slab determines its negative thermal buoyancy, which may affect significantly the dynamics of slab subduction. Many reseachers have studied the effects of slab age on its subduction dynamics (e.g., Capitanio et al., 2007; Capitanio, 2013; Garel et al., 2014; Ribe, 2010; Agrusta et al., 2017; Crameri and Lithgow-Bertelloni, 2018; Chen et al., 2022). They found that, in general, the older a subducting slab is, the greater its density and intensity become, and consequently, the larger its negative thermal buoyancy and subduction velocity in the mantle, which favors the slab's subduction into the deep mantle. Accordingly, compared to a younger slab, an older slab reaches the 660-km interface faster and is more likely to cause both trench retreat and the penetration of the 660-km interface into the lower mantle. When a younger slab arrives at the 660-km discontinuity, it may initially fold or buckle within the MTZ for a certain period due to resistance from the post-spinel transition and the increase in viscosity, but it eventually penetrates the 660-km interface into the lower mantle. In contrast, an older slab may initially penetrate the 660-km interface into the lower mantle, but afterwards bend and lie down above the interface, stagnating wihin the MTZ for a certain period, and eventually penetrate the interface into the lower mantle again. Obviously, the seafloor age (t_o) derived from the plate reconstruction of Müller et al. (2016) has uncertainty. Therefore, in order to probe the effects of slab age on the Pacific slab subduction dynamics, we have established several geodynamic models in which the slab's ages are 50 %, 75 %, 100 %, 125 %, and 150 % of t_o, corresponding to the models M34, M35, M25, M36, and M37, respectively, as listed in Table 2.

These models predict a very similar structure but noticeably different

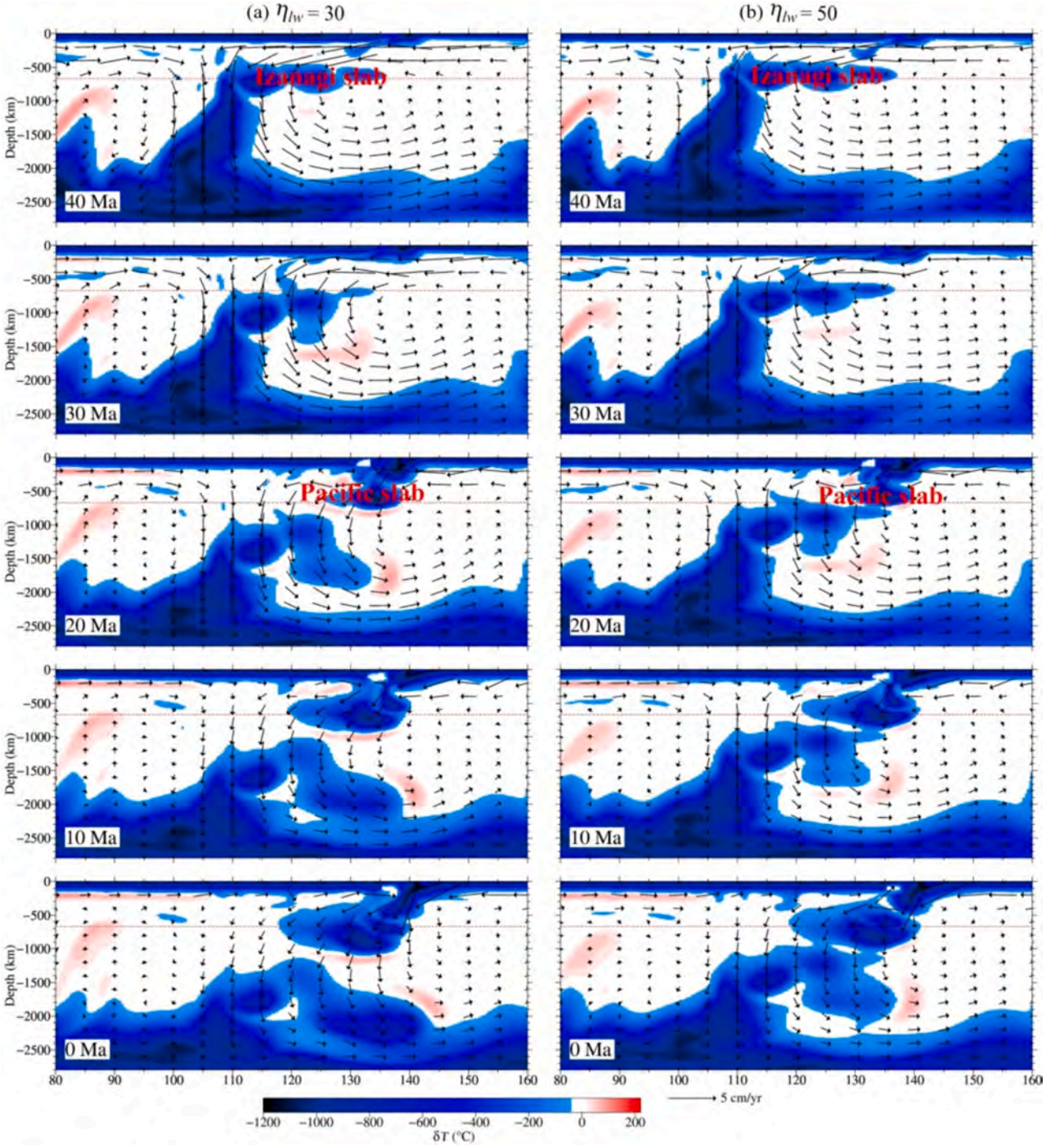

Fig. 6. Dynamic process of the Pacific slab subduction predicted by the models (a) M25 with $\eta_{lw} = 30$ and (b) M26 with $\eta_{lw} = 50$ along latitude 41.67°N.

westernmost positions and bottom depths of the Pacific slab in the modern mantle beneath the CVP (Fig. 9). The positions and bottom depths are 115.90°E and 965 km (M34), 117.02°E and 1025 km(M35), 117.94°E and 1100 km (M25), 118.19°E and 1160 km (M36), and 118.42°E and 1215 km (M37), respectively (Figs. 4h and 9). Accordingly, the westward movement distance decreases and sinking depth deepens gradually with increasing slab age. The maximum differences between the distances and the sinking depths predicted by these geodynamic models are ~210 km and ~ 250 km, respectively. These results indicate that a younger slab is more likely to stagnate in the MTZ and move westwardly a longer distance in the mantle, consistent with previous studies (e.g., Čížková and Bina, 2013; Zhong and Gurnis, 1997). All of the predicted westernmost positions are located to the west of the position (~120°E; Fig. 2) mapped by seismic tomography, indicating that the uncertainty in slab age does not significantly affect the prediction of the westernmost position of the Pacific slab beneath the CVP. However, the minimum sinking depth of ~950 km, corresponding to the model with half of t_0 (M34), is notably larger than the sinking depth (< 800 km; Fig. 2) of the modern Pacific slab beneath the CVP, suggesting that it is challenging to reproduce the sinking depth inferred from seismic tomography solely by varying the slab's age.

Slab age has a significant impact on the Pacific slab subduction dynamics beneath the CVP. Compared to an older slab, a younger slab is more conducive to breaking off, stagnating in the MTZ, and moving a

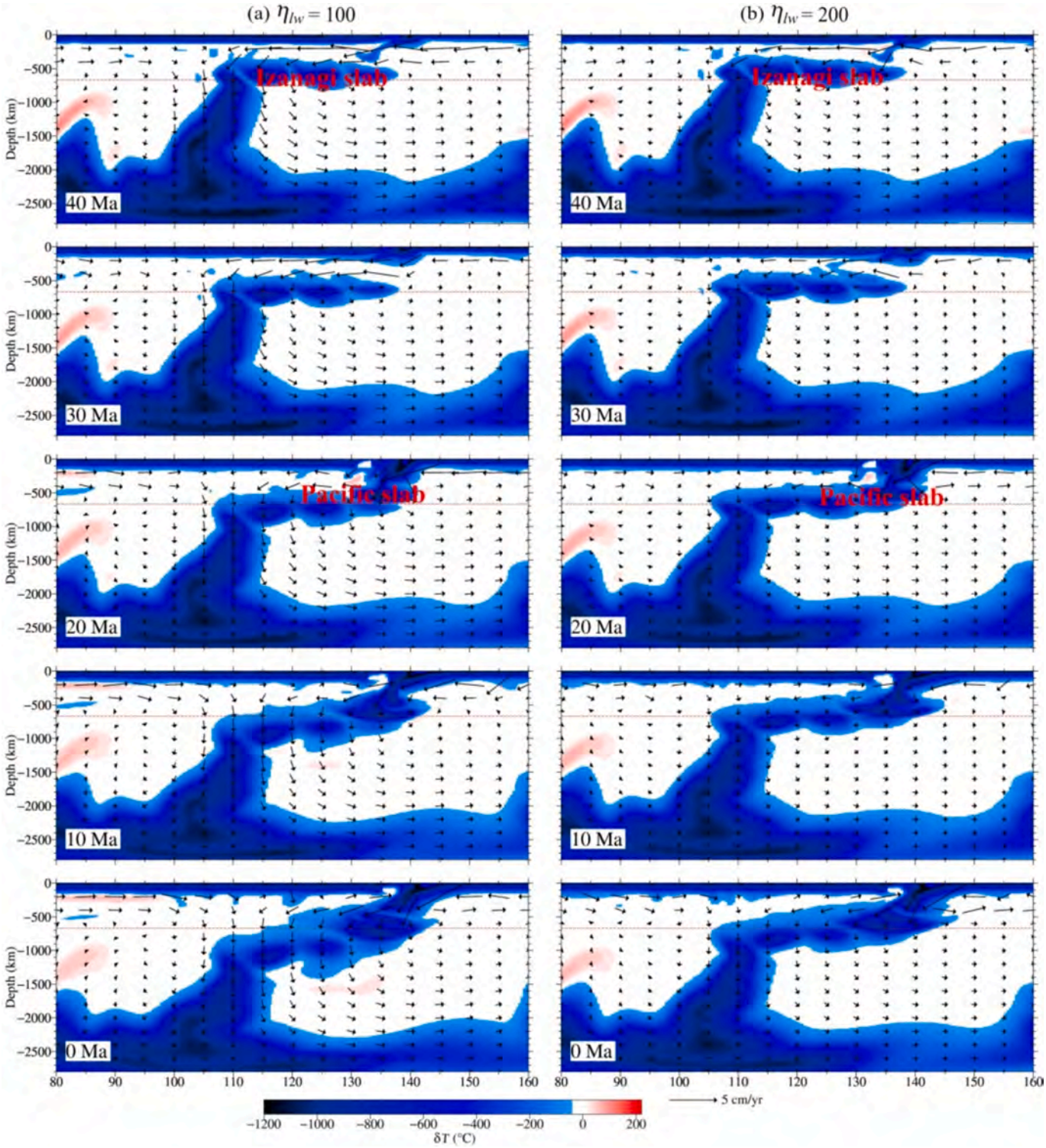

Fig. 7. Dynamic process of the Pacific slab subduction predicted by the models (a) M27 with $\eta_{lw} = 100$ and (b) M29 with $\eta_{lw} = 200$ along latitude 41.67°N.

longer distance westward (Fig. 10). Furthermore, a younger slab may cause more delamination of the continental lithosphere, and the delaminated lithosphere may adhere to the westernmost end of the Pacific slab (Fig. 10). Accordingly, a younger slab is more likely to reproduce the DCL on the west of the Pacific slab beneath the CVP, as inferred from seismic tomography (Fig. 2).

4.5. Effects of the viscosity in the MTZ

In this section, we probe the effects of the viscosity in the MTZ (η_{mtz}) on the dynamics of Pacific slab subduction beneath the CVP. Here we increase the η_{mtz} from 1.0 (M25) to 2.5 (M38), 5.0 (M39), 7.5 (M40) and 10 (M41) for our goal. These models predict a similar modern Pacific slab structure (Fig. 11). The westernmost positions and bottom depths are 117.94°E and 1100 km (M25), 117.42°E and 1115 km (M38), 117.11°E and 1120 km (M39), 116.77°E and 1105 km (M40), and

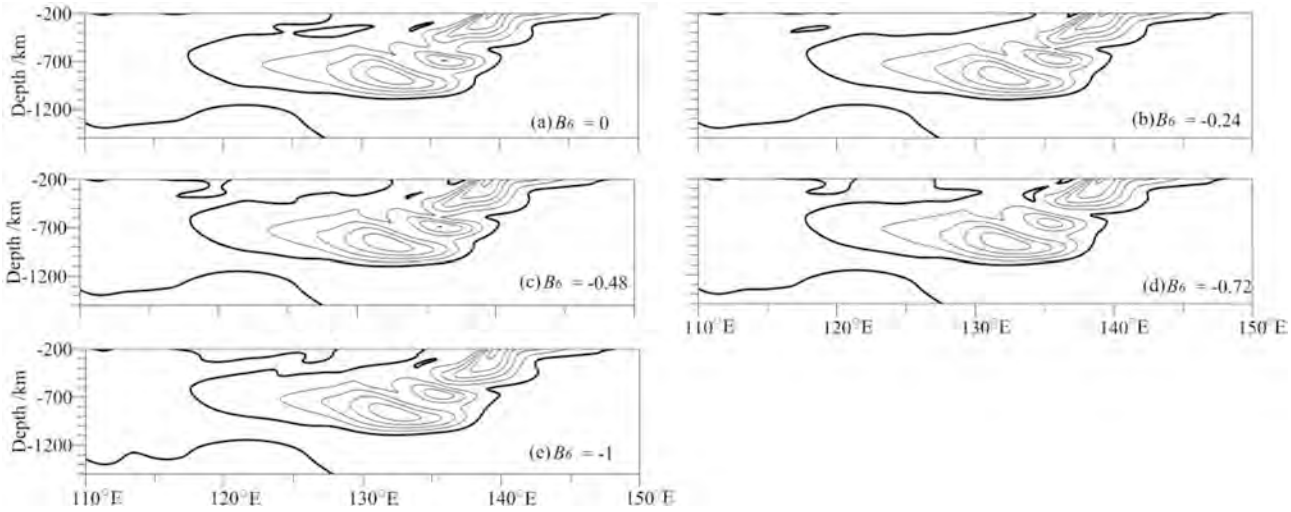

Fig. 8. Present-day (0 *Ma*) Pacific slab structure in the mantle predicted by the models M25 and M30 – M33. The thick line stands for the −50 °C isotherm. The isotherm interval is 200 degrees Celsius.

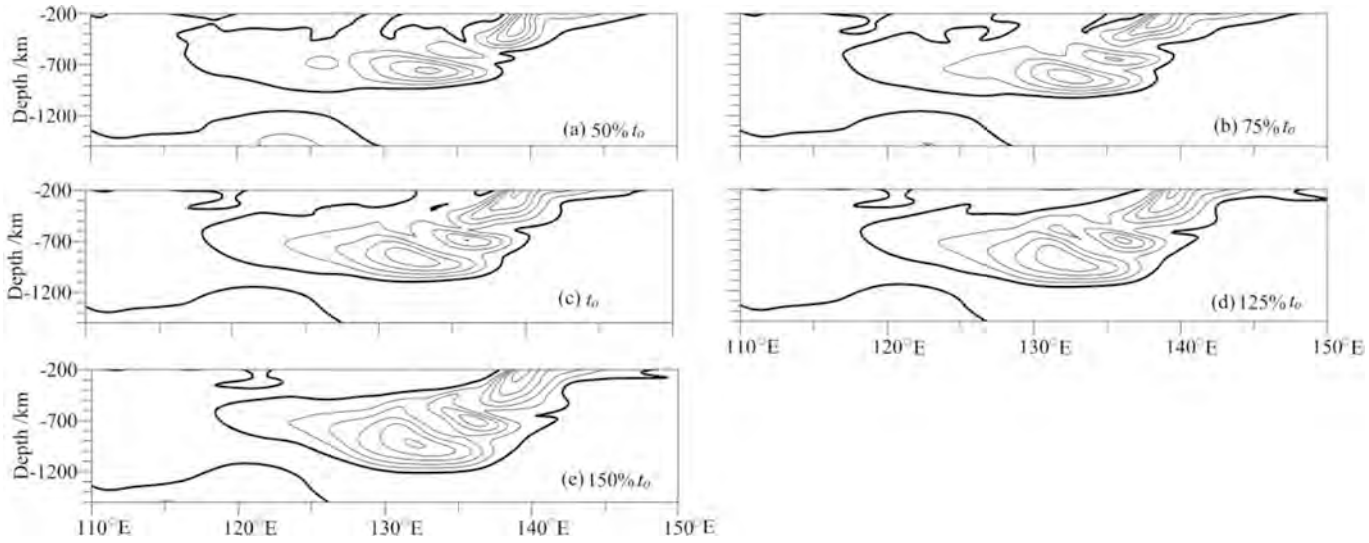

Fig. 9. Present-day (0 *Ma*) Pacific slab structure in the mantle predicted by the geodynamic models that incorporate varying slab ages. The thick line stands for the −50 °C isotherm. The isotherm interval is 200 degrees Celsius.

116.65°E and 1100 km (M41), respectively (Figs. 4i and 11). It is seen that, as η_{mtz} increases, the westward movement distance consistently increases, whereas the sinking depth initially deepens and subsequently becomes shallower. The maximum difference is ~105 km between the distances and ~ 20 km between the sinking depths predicted by these geodynamic models. These results indicate the η_{mtz} has minor effects on the structure and sinking depth of the Pacific slab, but more pronounced effects on its westward movement distance. It is clearly observed that as η_{mtz} increases, there is an increasing amount of continental lithosphere delamination (Figs. 12 and 13). The delaminated lithosphere may attach to the top (at $\eta_{mtz} = 5.0$; M39) or both the top and westernmost end (at $\eta_{mtz} \geq 7.5$; M40 – M41) of the Pacific slab (Fig. 13). Accordingly, a larger η_{mtz} is favorable to predicting the DCL inferred seismically (Fig. 2). However, an increased η_{mtz} does not adequately reproduce both the Pacific slab and the DCL on its western side, as all predicted westernmost positions are significantly distant (> 200 km) from the seismically inferred position (~114°E) on its east side (Fig. 2). Furthermore, all predicted bottom depths are considerably deeper (> 400 km) than the seismic inference (Fig. 2), and a mantle wedge does not form due to the connection of the continental lithosphere with both the slab and the DCL (Fig. 13).

4.6. *Effects of the viscosity in the middle part of the lower mantle*

Some studies have pointed out that, with increasing depth, the viscosity of the lower mantle increases gradually, reaching a maximum close to 2000 km, and then decreases gradually (e.g., Forte et al., 2010; Mitrovica and Forte, 2004; Steinberger and Calderwood, 2006; Ricard and Bai, 1991). Accordingly, in this section, we increase the viscosity (η_{mlw}) in the middle part of the lower mantle, ranging from 1500 to 2500 km, from 30 (M25) to 50 (M42), 100 (M43) and 150 (M44), in order to probe its effects on the Pacific slab subduction dynamics beneath the CVP. The westernmost positions and bottom depths are approximately 117.94°E and 1100 km (M25), 117.88°E and 1070 km (M42), 118.57°E and 1025 km (M43), and 118.84°E and 995 km (M44), respectively (Figs. 4j and 14). The maxmimum difference is approximately 80 km for the former and 105 km for the latter. These results indicate that the η_{mlw} has noticeable effects on both the westward movement distance and sinking depth of the Pacific slab. As η_{mlw} increases, its sinking depth decreases at all times, while the distance increases slightly at first for

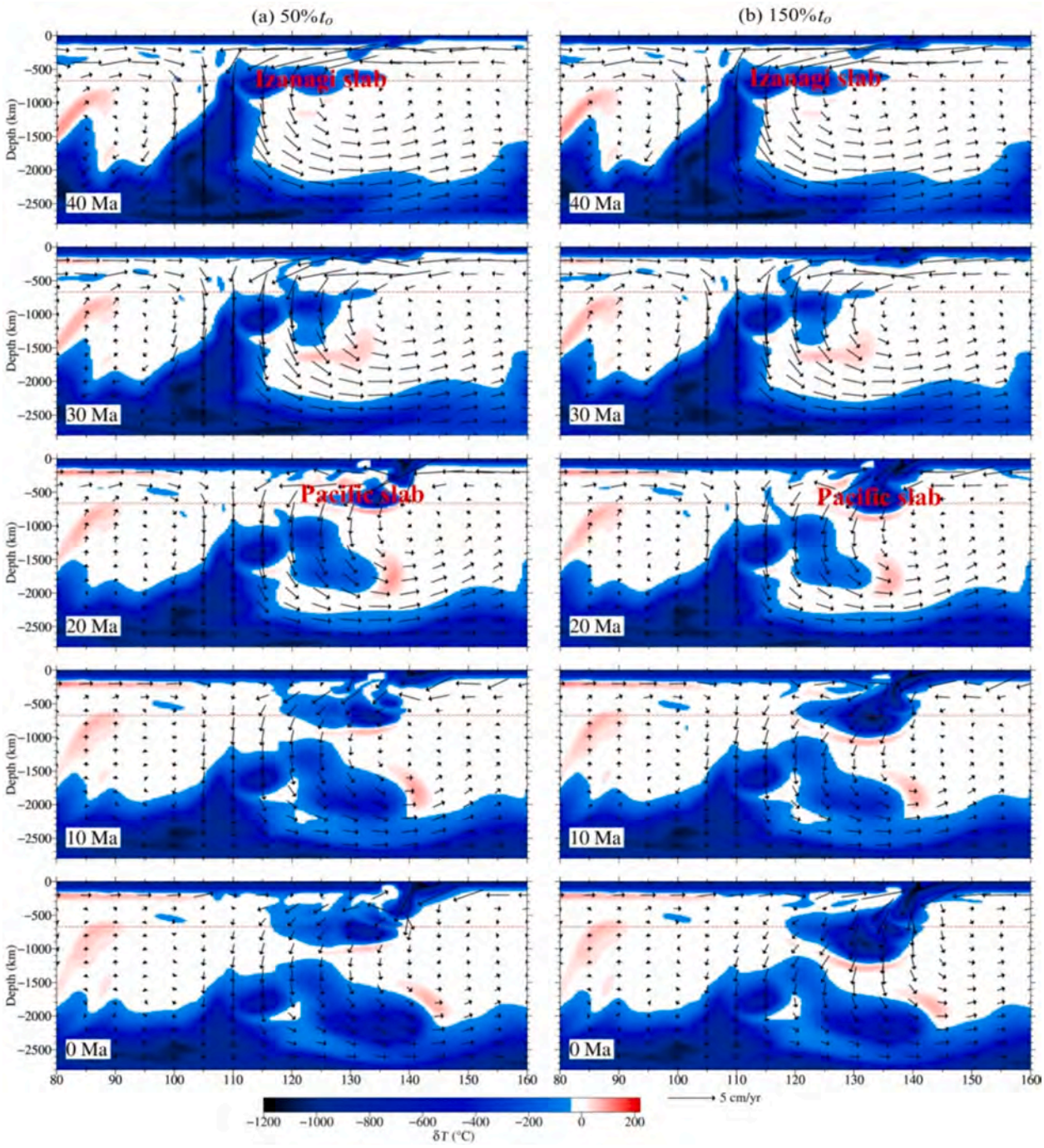

Fig. 10. Dynamic process of the Pacific slab subduction predicted by the models (a) M34 with slab age of 50 % t_o, and (b) M37 with slab age of 150 % t_o along latitude 41.67°N.

small η_{mlw} ($\leq$ 50) and then decreases for large η_{mlw} ($\geq$ 100). All of the westernmost positions are located to the west of the seismic inference (~120°E; Fig. 2), suggesting that the geodynamic models that incorporating varying η_{mlw} may predict the westernmost position of the Pacific slab well. However, all of bottom depths are significantly deeper than the seismic inference ($\leq$ 800 km; Fig. 2), implying that it is challenging to reasonably reproduce its sinking depth.

The Pacific slab arrives at the 660-km discontinuity at ~20 *Ma* in all of these models (Figs. S8 and S9). Since the increase in the η_{mlw} reduces the sinking velocity of the Izanagi slab, and the sinking depth consequently becomes shallower. When $\eta_{mlw} \geq$ 100 (M43 - M44), since the Izanagi slab sinks slow down significantly, unlike the situation for a small η_{mlw} ($\leq$ 50; Fig. S8), the slab does not sink below the Pacific slab. Consequently, the westernmost end of the Pacific slab comes into contact with the easternmost end of the Izanagi slab at ~20 *Ma* (Fig. S9). This situation not only causes the bottom of the Pacific slab to contact the top of the Izanagi slab in the modern mantle (Figs. 14c and d), but also slows down the westward movement of the Pacific slab, which may be the main reason for its predicted westernmost positions being closer to the east in the modern mantle compared to a small η_{mlw} ($\leq$ 50) (compare Fig. 14a, b and Fig. 14c, d). Therefore, the geodynamic models with large η_{mlw} ($\geq$ 100) do not reproduce the result that the Izanagi slab is located below, rather than in contact with, the Pacific slab, as inferred from global seismic models such as MIT08 (Li et al., 2008; Li and van der

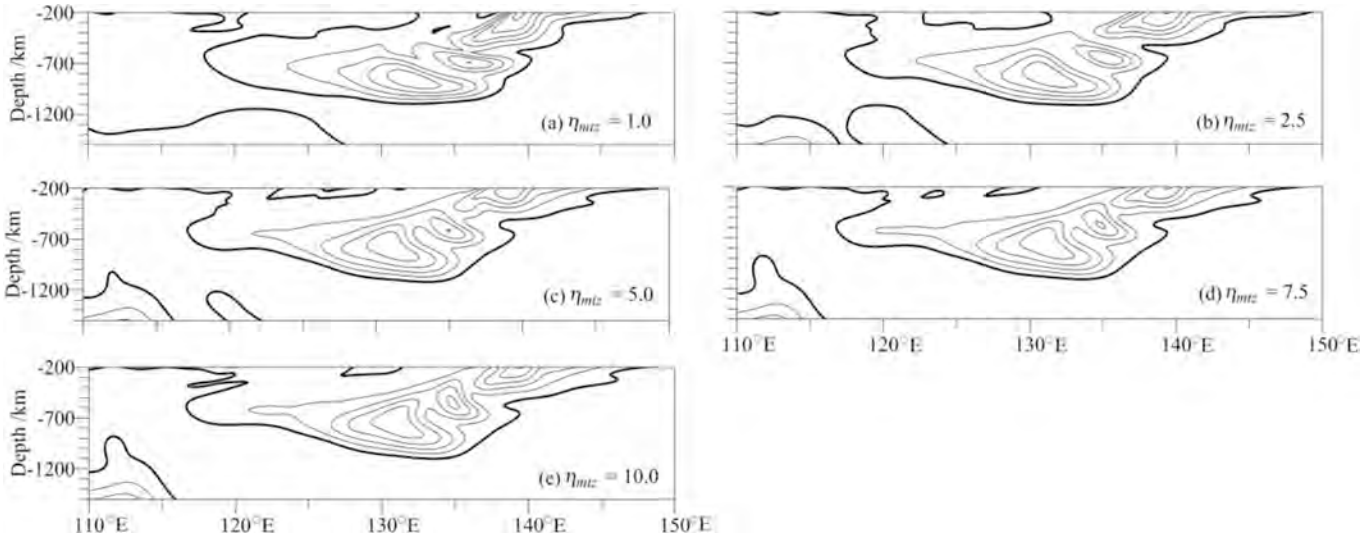

Fig. 11. Present-day (0 *Ma*) Pacific slab structure in the mantle predicted by the geodynamic models that incorporate varying viscosities in the MTZ. The thick line stands for the −50 °C isotherm. The isotherm interval is 200 degrees Celsius.

Hilst, 2010), LLNL_G3Dv3 (Simmons et al., 2012), TX2019slab (Lu et al., 2019), and GAP_P4 (Obayashi et al., 2013; Fukao and Obayashi, 2013) (Fig. S4). Aditionally, all of the models with different η_{mlw} predict the delamination of the continental lithosphere during the subduction of the Pacific slab, but the delamination is sporadic, and the delaminated lithosphere does not attach to the westernmost end of the Pacific slab (Figs. S8 and S9). Thus η_{mlw} is not a key parameter for predicting the DCL whose westernmost postion is located at ~114°E (Fig. 2).

4.7. Effects of the oceanic asthenosphere density

It is generally assumed in most studies on slab subduction dynamics that the oceanic asthenosphere possesses the same density and composition as the underlying mantle. In other words, the oceanic asthenosphere and its underlying mantle exhibit similar thermal and compositional buoyancy characteristics (e.g., Zhong and Gurnis, 1995; Billen, 2008; Liu and Stegman, 2011; Faccenda and Capitanio, 2013). The geodynamic models based on this assumption consistently predict a continuous downward flow in the subslab region, indicating the entrainment of vast amounts of oceanic asthenosphere material reaching deep into the mantle. However, upwelling hot mantle plumes may result in a hotter and less viscous oceanic asthenosphere compared to the underlying mantle. Typically, its temperature may be 100–200 °C higher, and consequently, its density and viscosity are approximately 0.5–1.0 % and 2–3 orders of magnitude lower, respectively (Morgan et al., 2007). Morgan et al. (2007) discovered that only a small quantity of asthenosphere material (approximately 30 km thick) could recycle into the deep mantle following a subducting slab, using both analog and numerical models that incorporated a hotter and less viscous oceanic asthenosphere (in comparison to the underlying ambient mantle). Subsequently, Liu and Zhou (2015) found that significantly more asthenosphere material (exceeding 100 km thick) could be entrained into the deep mantle, based on geodynamic models that employed an oceanic asthenosphere density anomaly ($\Delta\rho_{asth}$) of −0.5 % to −2 % (corresponding to approximately 600 °C hotter than the underlying mantle) and a viscosity anomaly ($\Delta\eta_{asth}$) up to 3 orders of magnitude lower. Liu and Zhou (2015) further proposed that the more negative the $\Delta\rho_{asth}$ (i.e., the lower the density or the higher the temperature of the oceanic asthenosphere relative to the underlying mantle) or the smaller the $\Delta\eta_{asth}$ (i.e., the higher the viscosity of the oceanic asthenosphere), the smaller the dip angle of a subducting slab, making the slab flatter. However, the effects of $\Delta\eta_{asth}$ are considerably smaller than those of $\Delta\rho_{asth}$. Additionally, these are two-dimensional models that not only fail to predict the toroidal flow accompanying a subducting slab but also neglect specific scenarios, such as paleoplate motions, seafloor age, and trench positions, in the context of Pacific plate subduction. Accordingly, here we simulate the effects of the oceanic asthenosphere density using geodynamic models the data assimilation, in which $\Delta\rho_{asth} = 0 \sim -3$ %, corresponding to the models M25 and M45 – M47 (Table 2). These $\Delta\rho_{asth}$ values imply that the temperature of the oceanic asthenosphere is approximately 0–1000 °C higher than that of the underlying mantle. It is unreasonable to assume that the oceanic asthenosphere is 1000 °C hotter than the underlying mantle, but it provides us with an opportunity to explore extreme situations.

The Pacific slab structures in the modern mantle, as predicted by the models M25 and M45 - M47, exhibit a minimum correlation coefficient of 0.89 (Table S4). This indicates that these models predict very similar Pacific slab structures, suggesting that $\Delta\rho_{asth}$ has minimal effects on the predicted structures. The westernmost positions and bottom depths are approximately 117.94°E and 1100 km (M25), 116.91°E and 1110 km (M45), 116.41°E and 1110 km (M46), and 116.29°E and 1100 km (M47), respectively (Figs. 4k and 15). This result indicates that $\Delta\rho_{asth}$ has a certain degree of effect on the westward movement distance of the Pacific slab but almost no effect on its sinking depth in the mantle. The more negative the $\Delta\rho_{asth}$, the longer the westward movement distance, but the smaller the increase of the distance. Specially, an increase in $\Delta\rho_{asth}$ from 0 to −1 %, −1 % to −2 % and − 2 % to −3 % leads to an increase in the distance by 85 km, 40 km and 10 km, respectively. Therefore, an increase in the density constrast between the oceanic asthenosphere and its underlying mantle (i.e., a more negative $\Delta\rho_{asth}$) may moderately increase the westward movement distance of the Pacific slab but does not make its sinking depth shallower. All of these models (M25, M45 - M47) predict that the westernmost positions of the Pacific slab are further west than those observed seismically (~120°E; Fig. 2), and the bottom depths are deeper than 1100 km, which are significantly greater than those observed seismically (< 800 km). Furthermore, they fail to predict the DCL on the west of the Pacific slab, as inferred from seismic imaging (Fig. 2).

The subduction process of the Pacific slab, as predicted by these models, has generally been similar since 40 *Ma* (Figs. S10 and S11). As $\Delta\rho_{asth}$ becomes more negative, the positive thermal buoyancy attached to the Pacific slab increases, resulting in a generally smaller dip angle of the slab. However, upon comparing Fig. S10 and Fig. S11, we observe that the dip angle does not change strikingly, and at least the change is not more noticeable than that reported by Liu and Zhou (2015). We infer that this is due to the influence of the Izanagi slab, which exists in the

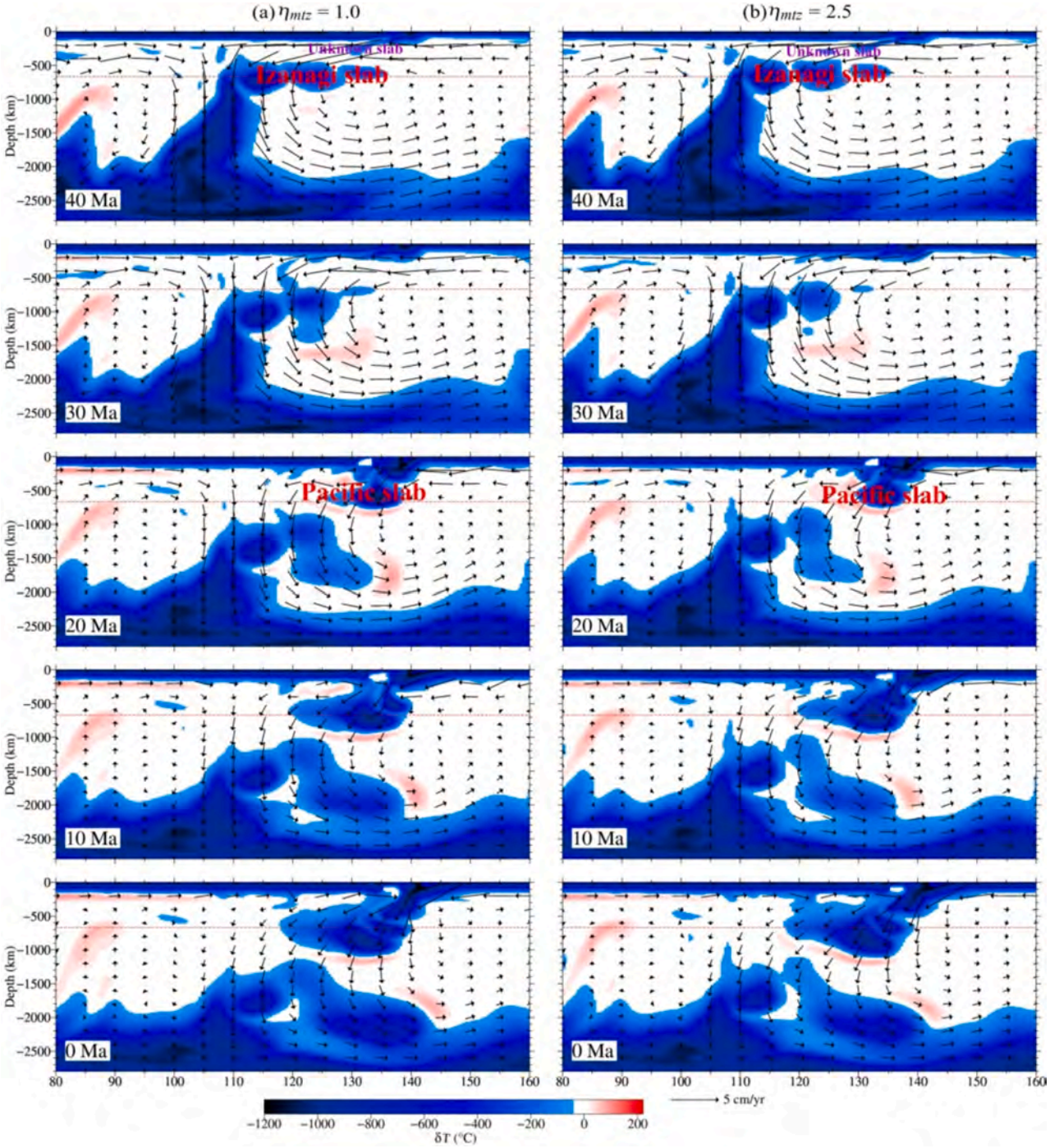

Fig. 12. Dynamic process of the Pacific slab subduction predicted by the models (a) M25 with η_{mtz} = 1.0 and (b) M38 with η_{mtz} = 2.5 along latitude 41.67°N.

mantle prior to the subduction of the Pacific slab. It is also observed from Figs. S10 and S11 that a more negative $\Delta\rho_{asth}$ would lead to stronger lithosphere delamination at ~20 *Ma*. Howbeit, all of these delamination materials adhere to the top rather than the westernmost end of the Pacific slab. Perhaps this is the reason why these models do not predict the DCL on the west of the Pacific slab, as inferred from seismic imaging.

4.8. *Effects of density jump across the 660-km discontinuity*

It has been inferred that mantle density increases by 3.8 % - 10.2 % across the 660-km discontinuity (Wang et al., 2023; Castle and Creager, 2000; Deuss, 2009; Dziewonski and Anderson, 1981; Estabrook and Kind, 1996; Kato and Kawakatsu, 2001; Lau and Romanowicz, 2021; Matsui, 2001; Montagner and Anderson, 1989; Morelli and Dziewonski, 1993; Shearer and Flanagan, 1999; Yu et al., 2018). This increase in density affects the behavior of a subducting slab. Christensen and Yuen (1984) employed a two-dimensional finite element model of time-dependent convection to study the effects of the density jump ($\Delta\rho_{660}$) across the 660-km discontinuity on slab subduction dynamics. They discovered that when $\Delta\rho_{660} \geq 5$ %, a subducting slab may primarily stagnate within the MTZ, leading to a depression of 50–200 km in the discontinuity; when 2 % $\leq \Delta\rho_{660} \leq$ 5 %, the slab likely partially penetrates the discontinuity and plunges several hundred kilometers into the lower mantle; and when $\Delta\rho_{660} \leq$ 2 %, the slab probably directly

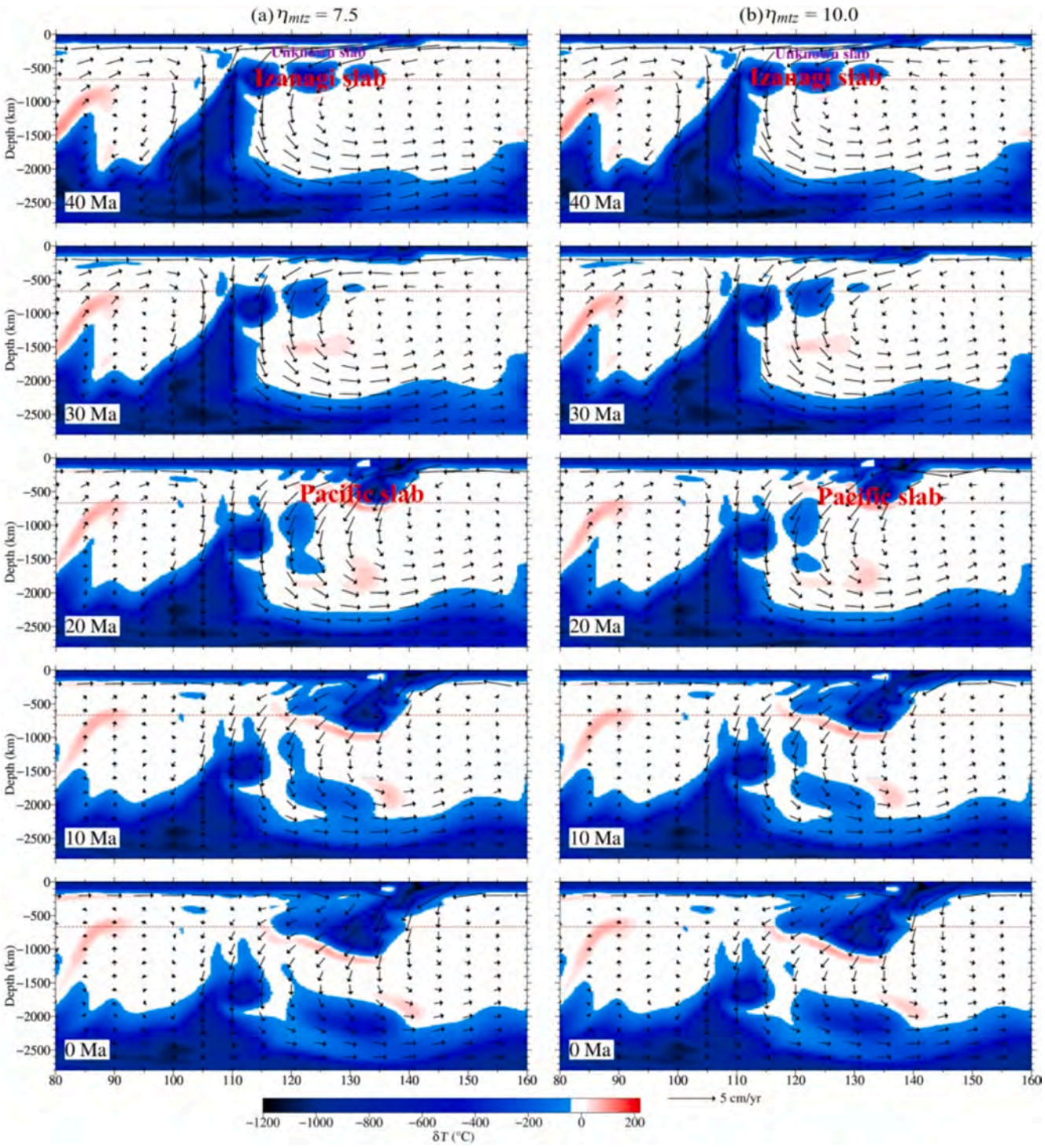

Fig. 13. Dynamic process of the Pacific slab subduction predicted by the models (a) M40 with η_{mtz} = 7.5 and (b) M41 with η_{mtz} = 10.0 along latitude 41.67°N.

penetrates the discontinuity and does not stop before arriving at the core-mantle boundary. The analogue models presented by Kincaid and Olson (1987) demonstrated that the penetration of a subducting slab through the 660-km discontinuity is controlled by the ratio of the densities of the slab (ρ_S), upper mantle (ρ_U) and lower mantle (ρ_L), defined as $R = (\rho_S - \rho_L)/(\rho_S - \rho_U)$. When $R \geq 0.5$, which corresponds to $\Delta\rho_{660} \leq 2$ % in the study by Christensen and Yuen (1984), a subducting slab penetrates the 660-km discontinuity nearly vertically and directly into the lower mantle; when $-0.2 \leq R \leq 0.5$, corresponding to 2 % $\leq \Delta\rho_{660} \leq 5$ % in Christensen and Yuen (1984), the slab partially penetrates the discontinuity; and when $R \leq -0.2$, corresponding to $\Delta\rho_{660} \geq 5$ % in Christensen and Yuen (1984), there is little to no penetration of the discontinuity by the slab. These results indicate that the increased density across the discontinuity results in an increase in positive buoyancy attached to a subducting slab. The larger the $\Delta\rho_{660}$, the greater the positive buoyancy, and consequently, the probability increases for the stagnation of the slab arriving at the 660-km discontinuity in the MTZ. Accordingly, we study the effects of $\Delta\rho_{660}$ on the behavior of the Pacific plate subduction. Given that $\Delta\rho_{660}$ ranges between 3.8 % and 10.2 %, we assume $\Delta\rho_{660}$ = 4 %, 8 %, 10 %, and 15 %, corresponding to the models M48, M25, M49 and M50, as listed in Table 2.

The models M48, M25, M49 and M50 predict a similar present-day

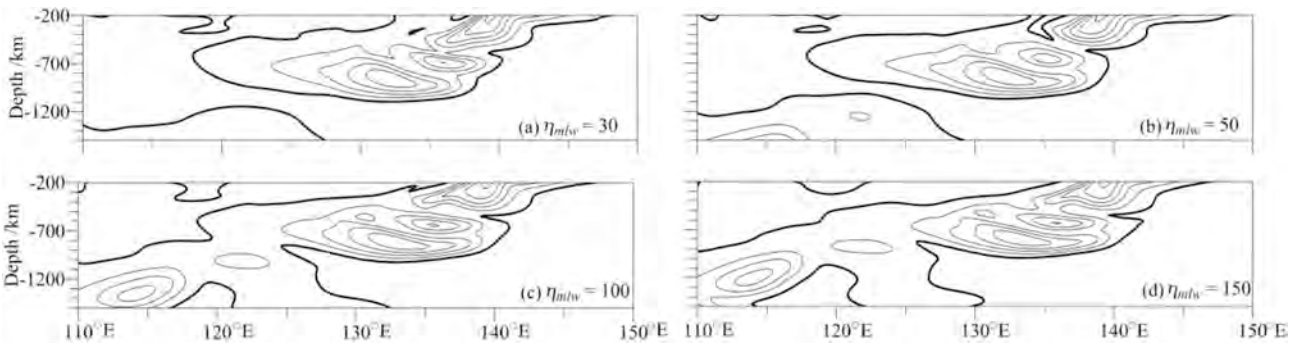

Fig. 14. Present-day (0 *Ma*) Pacific slab structure in the mantle predicted by the geodynamic models that incorporate varying viscosities in the middle part of the lower mantle. The thick line stands for the −50 °C isotherm. The isotherm interval is 200 degrees Celsius.

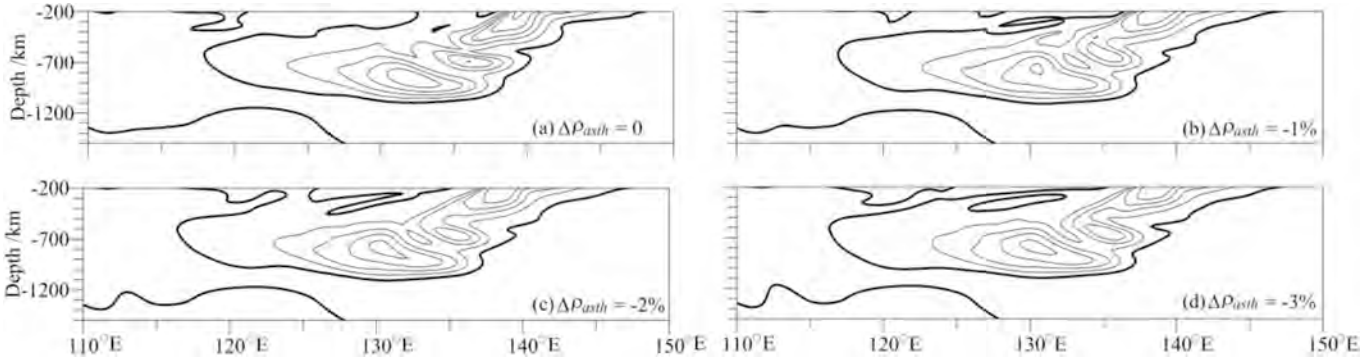

Fig. 15. Present-day (0 *Ma*) Pacific slab structure in the mantle predicted by the geodynamic models that incorporate varying density anomalies of the oceanic asthenosphere. The thick line stands for the −50 °C isotherm. The isotherm interval is 200 degrees Celsius.

structure of the Pacific slab. However, because of the significant differences in westward movement distance and sinking depth, especially the latter, the cross-correlation coefficients exhibit large variations (Table S5). The predicted westernmost positions and bottom depths are approximately 119.78°E and 1375 km (M48), 117.94°E and 1100 km (M25), 116.20°E and 960 km (M49), and 116.08°E and 780 km (M50), respectively (Figs. 4l and 16). This result implies that as $\Delta\rho_{660}$ increases, the westward movement distance of the Pacific slab increases notably, and the sinking depth becomes significantly shallower. In other words, the increase of $\Delta\rho_{660}$ enhances the probability of slab stagnation within the MTZ and reduces the likelihood of the Pacific slab penetrating the 660-km discontinuity into the lower mantle, which is consistent with the previous studies (Christensen and Yuen, 1984; Kincaid and Olson, 1987). An increase in $\Delta\rho_{660}$ from 4 % to 15 % leads to an increase in the westward movement distance of ~300 km and a decrease in the sinking depth of ~600 km. As mentioned earlier, this is the primary reason for the significant difference in cross-correlation coefficients between the predictions of the geodynamic models with varying $\Delta\rho_{660}$. In addition, when $\Delta\rho_{660}$ equals 15 %, the predicted bottom depth of the Pacific slab is ~780 km, which is consistent with the depth inferred from seimic models. Meanwhile, the westernmost position (~116.08°E) of the Pacific slab predicted by the model with $\Delta\rho_{660}$ = 15 % is further west than the seismic inference (~120°E; Fig. 2). Accordingly, the model may predict the Pacific slab well.

The models with different $\Delta\rho_{660}$ predict a similar subduction process of the Pacific slab since 40 *Ma* (Figs. 17 and 18). When $\Delta\rho_{660}$ is too high (e.g., 15 %), similar to having an excessively high lower mantle viscosity (Fig. 7), it results in a significant decrease in the sinking depth, which aligns more closely with seismic inference. However, this also leads to a noticeable decrease in the sinking velocity of the Izanagi slab.

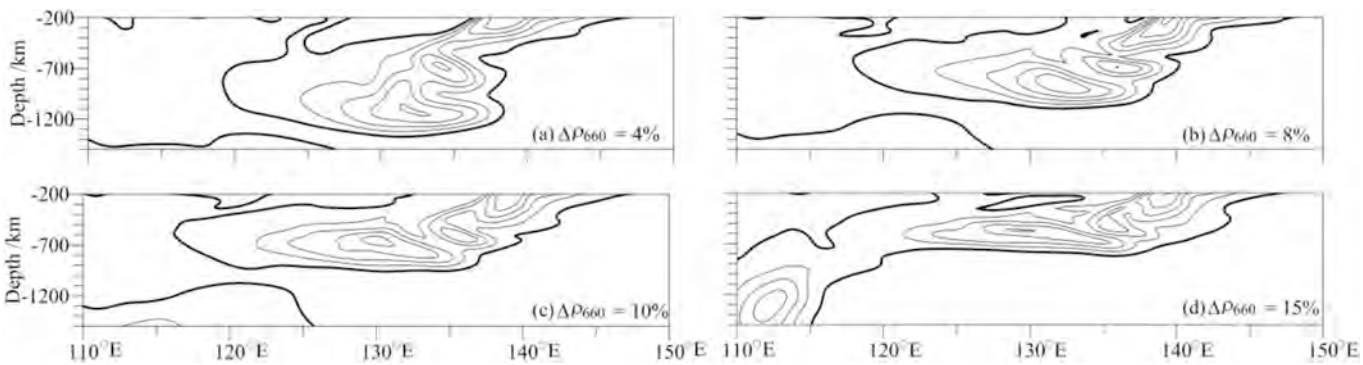

Fig. 16. Present-day (0 *Ma*) Pacific slab structure in the mantle predicted by the geodynamic models that incorporate varying density jumps across the 660-km discontinuity. The thick line stands for the −50 °C isotherm. The isotherm interval is 200 degrees Celsius.

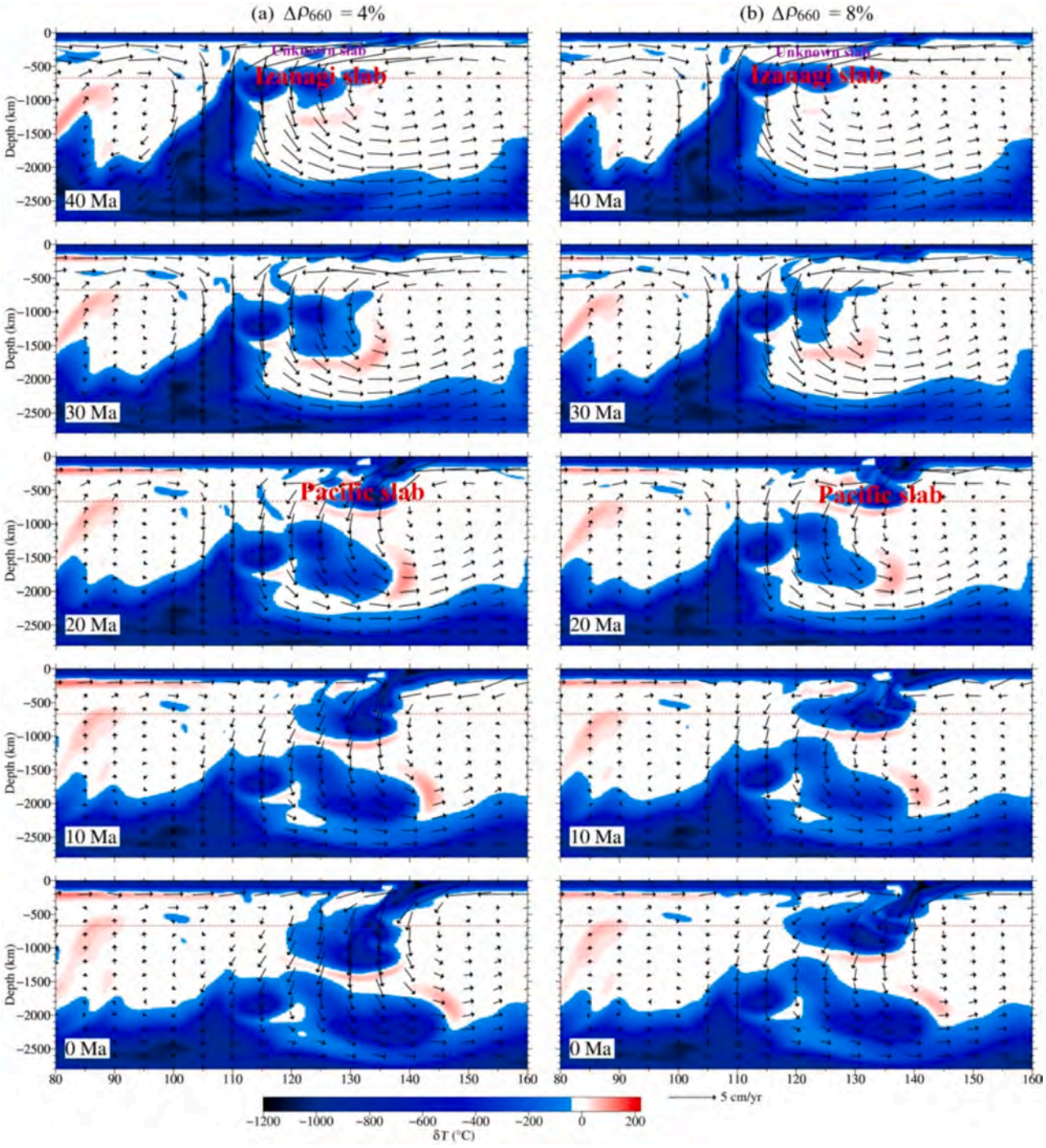

Fig. 17. Dynamic process of the Pacific slab subduction predicted by the models (a) M48 with $\Delta\rho_{660} = 4$ % and (b) M25 with $\Delta\rho_{660} = 8$ % along latitude 41.67°N.

Consequently, the westernmost end of the Pacific slab contacts with the easternmost end of the Izanagi slab at ~10 *Ma* (Fig. 18), which is inconsistent with the observation of the Izanagi slab sinking below the Pacific slab as revealed by global seismic tomography (Fig. S4; Li et al., 2008; Li and van der Hilst, 2010; Simmons et al., 2012; Lu et al., 2019; Obayashi et al., 2013; Fukao and Obayashi, 2013). Furthermore, as $\Delta\rho_{660}$ increases, the delamilation of continental lithosphere enhances, particularly at ~20 *Ma*, but these delamilated lithosphere adhere to the top rather than the westernmost end of the Pacific slab (Figs. 17 and 18). Therefore, it struggles to predict the DCL as shown in Fig. 2 for geodynamic models with varying $\Delta\rho_{660}$.

5. Remarks and suggested parameters

As depicted in Section 2, the high-speed anomaly zone is inferred to be caused by the Pacific slab in its eastern part and the DCL in its western part. Therefore, a reasonable geodynamic model should reproduce both the Pacific slab and the DCL, which contacts with its westernmost end, as shown in Fig. 2. The results in Section 4 suggest that it is relatively straightforward to well reproduce the westernmost position of the Pacific slab, as nearly all models listed in Table 2 are capable of doing so. However, predicting the DCL and the sinking depth of the Pacific slab is more challenging. Accordingly, we provide our remarks and suggestions on the parameters to reproduce the sinking depth and the DCL here.

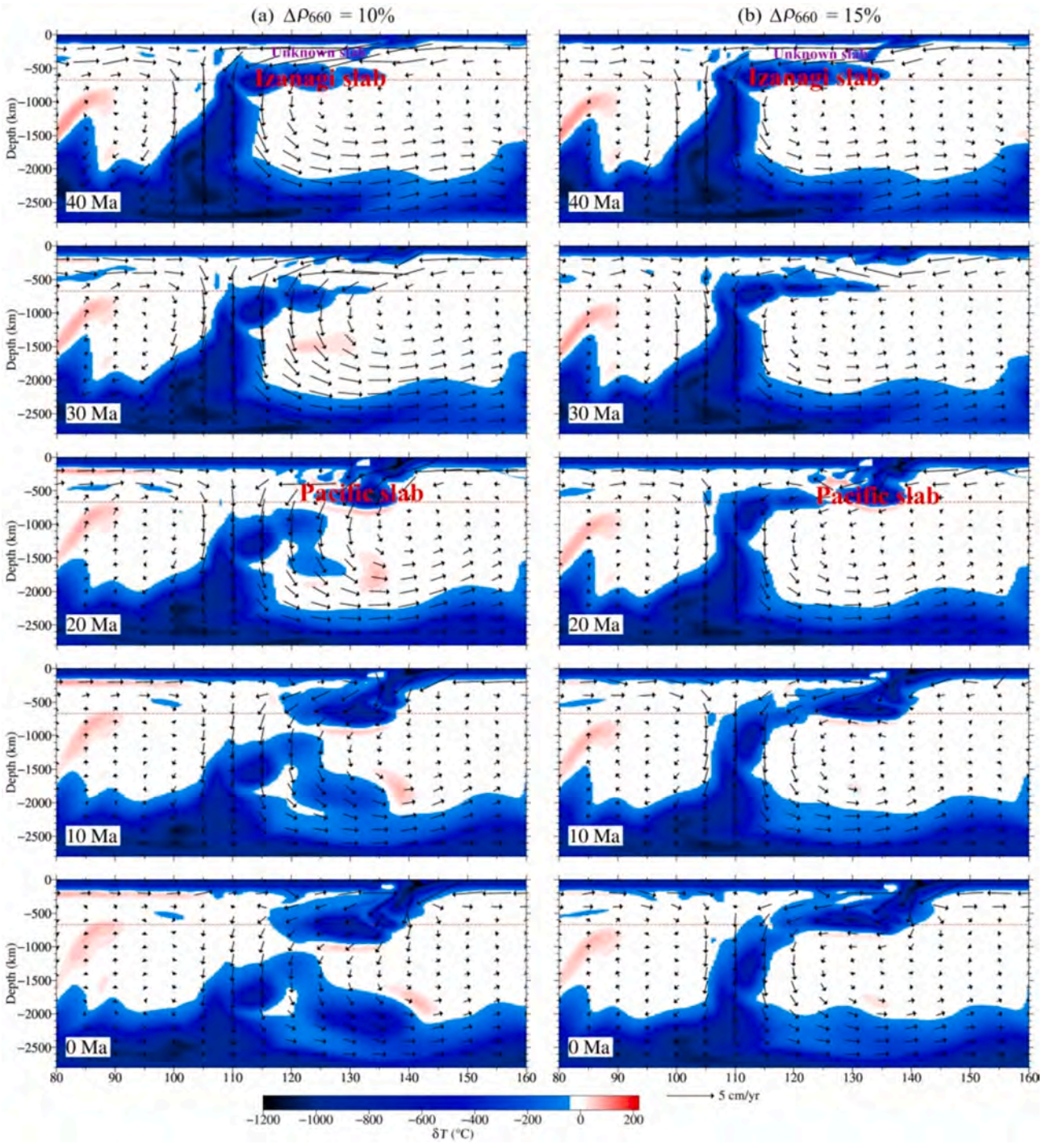

Fig. 18. Dynamic process of the Pacific slab subduction predicted by the models (a) M49 with $\Delta\rho_{660} = 10$ % and (b) M50 with $\Delta\rho_{660} = 15$ % along latitude 41.67°N.

Compared with the γ_{660}, the effect of the γ_{410} is secondary. The γ_{410} has minor effects on the westward movement distance and slight effects on the sinking depth of the Pacific slab in the mantle. In general, as γ_{410} increases, the westward movement distance decreases, and the sinking depth becomes gradually deeper. With the increase of the $|\gamma_{660}|$, the effect of the γ_{410} gradually weakens. When $|\gamma_{660}| \geq 4$ MPa/K, its effects can be ignored. The γ_{660} has significant effects on both the westward movement distance and the sinking depth of the Pacific slab in the mantle. When $|\gamma_{660}| \leq 5$ MPa/K, the westward movement distance increases, while the opposite occurs when $|\gamma_{660}| > 5$ MPa/K. However, the sinking depth always becomes significantly shallower with the increasing $|\gamma_{660}|$. The maximum differences exceed 300 km and 600 km, respectively, for the westward movement distance and the sinking depth within the range of γ_{660} between −1 and − 6 MPa/K. When $|\gamma_{660}| \geq 5$ MPa/K, the main part of the Pacific slab may stagnate in the MTZ. Both δh_{410} and δh_{660} slightly affect the dynamic process and structure of the Pacific slab. All of the geodynamic models with different γ_{660} or γ_{410} cannot predict the DCL. However, the model with a larger γ_{660} and a smaller γ_{410} favors a better prediction of the sinking depth of the Pacific slab. Additionally, though our modeling implies $|\gamma_{660}| \geq 5$ MPa/K, considering that the γ_{660} ranging from −1.5 to −3 MPa/K have been used in previous predictions of the stagnant Pacific slab beneath East Asia (Ma et al., 2019; Mao and Zhong, 2018; Yang et al., 2018; Peng et al., 2021a), and the γ_{660} ranging from −2.5 to −3 MPa/K have been

inferred from seismic observations (Lebedev et al., 2002; Fukao et al., 2009), we suggest that γ_{660} is best within the range of −2.0 to −3 MPa/K.

The viscosity in the lower mantle (η_{lw}) notably affects both the westward movement distance and sinking depth of the Pacific slab. The maximum differences exceed 200 km and 300 km, respectively, for the sinking depth and distance over a range of η_{lw} from 30 to 200. As η_{lw} increases, the sinking depth consistently becomes shallower, while the westward movement distance initially decreases and then increases. The predicted westernmost position of the Pacific slab is slightly further west than the seismic inference for low η_{lw} ($\leq$ 50), whereas the predicted bottom depth is notably deeper than that mapped by seismic tomography. A large η_{lw} ($\geq$ 100) may significantly reduce the sinking depth, but at the same time, it may result in the Izanagi slab obviously contacting the Pacific slab (Fig. 7), which is inconsistent with the seismic inference suggesting that the Izanagi slab has sunk below the Pacific slab (Fig. S4). Furthermore, this may lead to the predicted westernmost position being noticeably further east than the seismic inference. None of the models with different η_{lw} predict the DCL. Given that the model with a larger η_{lw} favors a better prediction of the sinking depth of the Pacific slab, and perhaps its westernmost postion, it is suggested that η_{lw} is best within the range of 30–50 and not exceed 75. The range of η_{lw} recommended here falls within but is significantly narrower than various ranges suggested in previous studies. These include ranges of 10–316 for interpreting the geoid anomalies (Hager, 1984; Hager et al., 1985; Hager and Richards, 1989; King and Masters, 1992; Ricard et al., 1993; Liu and Zhong, 2016; Liu et al., 2021), 1–100 for interpreting the variations in post-glacial sea-level (Cathles, 1975; Nakada and Lambeck, 1989; Tushingham and Peltier, 1992; Mitrovica and Peltier, 1993, 1995), 30–250 inferred from the inversion of convection-related observables (Forte and Mitrovica, 2001), 2–250 inferred from joint inversion of geoid/free-air gravity anomalies and post-glacial relative sea-level variations (Wu and Peltier, 1983; Forte and Mitrovica, 1996; Mitrovica and Forte, 1997; Paulson et al., 2007), and 30–100 constrained by slab dynamics (Liu et al., 2021).

The oceanic chemical layer has a bit of an effect on the westward movement distance but little effects on the sinking depth. The maximum differences are ~40 km and ~ 10 km, respectively, for the distance and sinking depth within the range of B_6 between 0 and − 1.0. As the chemical buoyance of the layer increases, that is, as B_6 becomes more negative, the westward movement distance of the Pacfic slab decreases initially and then increases. None of the models with different B_6 predict the DCL. Accordingly, the oceanic chemical layer does not play an important role in predicting the sinking depth of the Pacific slab and the DCL. It is suggested that B_6 may adopt a value of −0.48, which corresponds to the mean density of 3.0 g/cm^3 for the Earth's oceanic crust.

Slab age notably affects both the westward movement distance and sinking depth of the Pacific slab. The maximum differences are ~210 km and ~ 250 km, respectively, for the distance and sinking depth within the range of slab age between 50 %t_o and 150 %t_o. As slab age increases, the westward movement distance decreases, while the sinking depth gradually increases. This result implies that a younger slab is more conducive to stagnating in the MTZ and moving a longer distance westward. All of the geodynamic models with varying slab ages are unable to predict the DCL. Given that the model with a younger slab favors a better prediction of the sinking depth of the Pacific slab, it is suggested that the slab age is best to adopt the lower limit of the reconstructed seafloor age.

The viscosity in the MTZ (η_{mtz}) primarily influences the westward movement distance of the Pacific slab and has a slight effect on its sinking depth. It results in maximum differences of ~105 km and ~ 20 km, respectively, in the distance and sinking depth across a range of η_{mtz} from 1.0 to 10.0. As η_{mtz} increases, the distance initially increases and then decreases, while the sinking depth deepens initially and then become shallow. A larger η_{mtz} (e.g, 7.5) may lead to significant delamination of the continental lithosphere, and the delaminated lithosphere may attach to the westernmost end of the Pacific slab. Based on Magni and Király (2019), lithosphere delamination was divied into three groups: subducting plate delamination, peeling-off and dripping. We consider that the delamination discussed here belongs to the dripping or convective thinning type. This type is primarily caused by the Rayleigh-Taylor instability in compressional stress regimes (Magni and Király, 2019). Therefore, it may be appropriate to adopt a larger η_{mtz} when predicting the DCL on the western end of the Pacific slab. However, a larger η_{mtz} may also result in the connection of the continental lithosphere with the Pacific slab, ultimately leading to the absence of a noticeable mantle wedge. Consequently, it is suggested that, under comprehensive consideration, the η_{mtz} is better not to exceed 2.5.

The viscosity (η_{mlw}) in the middle part of the lower mantle has noticeable effects on both the westward movement distance and sinking depth of the Pacific slab. It results in maximum differences of ~80 km and ~ 105 km, respectively, in the distance and sinking depth across a range of η_{mlw} from 30 to 150. An increase in η_{mlw} leads to a decrease in both the westward movement distance and the sinking depth. However, a large η_{mlw} ($\geq$100), like a large η_{lw}, may lead to the noticeable decrease in sinking velocity of the Izanagi slab, and consequently cause the Izanagi slab to contact the Pacific slab. All of the geodynamic models with different η_{mlw} cannot predict the DCL. Since the model with a larger η_{mlw} favors a better prediction of the sinking depth of the Pacific slab, it is suggested that η_{mlw} is best within the range of 30–50 and not exceed 75. This suggested range of η_{mlw} is significantly narrower than those inferred from joint inversions of global convection-related observables and GIA data (4–226, Mitrovica and Forte, 2004; 14–333, Forte et al., 2010), comparable to those inferred from mineral physics and surface observations (29–64, Steinberger and Calderwood, 2006), and wider than those derived on the basis of global long wavelength geoid anomalies (8–45, Ricard and Bai, 1991) and the combination of geoid and GIA data (5–10, Forte and Mitrovica, 1996).

The oceanic asthenosphere density ($\Delta\rho_{asth}$) has a notable effect on the westward movement distance, but has almost no effect on the sinking depth of the Pacific slab. It results in maximum difference of ~140 km in the distance over a range of $\Delta\rho_{asth}$ from 0 to −3 %. As $\Delta\rho_{asth}$ becomes more negative, the westward movement distance increases. A more negative $\Delta\rho_{asth}$ (e.g, −2 %) may cause significant lithosphere delamination (i.e., dripping; Magni and Király, 2019), and the delaminated lithosphere may adhere to the westernmost end of the Pacific slab, indicating that the model with a more negative $\Delta\rho_{asth}$ favors predicting the DCL. Therefore, it is suggested that $\Delta\rho_{asth}$ may adopt a reasonable and more negative value.

The density jump across the 660-km discontinuity ($\Delta\rho_{660}$) significantly affects both the westward movement distance and sinking depth of the Pacific slab. An increase in $\Delta\rho_{660}$ leads to a noticeable decrease in the distance and sinking depth. An increase in $\Delta\rho_{660}$ from 4 % to 15 % leads to a maximum difference of ~300 km for the westward movement distance and ~ 600 km for the sinking depth. A larger $\Delta\rho_{660}$ (e.g, 15 %) leads to a significantly shallower sinking depth, while simultaneously facilitating the connection of the easternmost end of the Izanagi slab with the westernmost end of the Pacific slab. Additionally, a larger $\Delta\rho_{660}$ (e.g., 10 %) may lead to lithosphere delamination (i.e., dripping; Magni and Király, 2019), with the delaminated material potentially adhering to the westernmost end of the Pacific slab. In other words, the geodynamic model with a larger $\Delta\rho_{660}$ favors predicting both a reasonable sinking depth of the Pacific slab and the DCL. Therefore, it is suggested that $\Delta\rho_{660}$ may adopt a value of ~10 % but should not exceed 15 %. This suggested range of $\Delta\rho_{660}$ is notably beyond the previous inference of 3.8–10.2 % (Wang et al., 2023; Castle and Creager, 2000; Deuss, 2009; Dziewonski and Anderson, 1981; Estabrook and Kind, 1996; Kato and Kawakatsu, 2001; Lau and Romanowicz, 2021; Matsui, 2001; Montagner and Anderson, 1989; Morelli and Dziewonski, 1993; Shearer and Flanagan, 1999; Yu et al., 2018).

In summary, a geodynamic model with a larger $|\gamma_{660}|$, η_{lw}, η_{mlw}, and/or $\Delta\rho_{660}$ is beneficial for predicting a reasonable sinking depth of the

Pacific slab, while a model with a more negative $\Delta\rho_{asth}$ and/or a larger $\Delta\rho_{660}$ favors predicting the DCL.

CRediT authorship contribution statement

Tao Zhu: Writing – original draft, Methodology, Investigation, Funding acquisition, Conceptualization. **Diandian Peng:** Writing – original draft, Software, Resources, Methodology. **Lijun Liu:** Writing – original draft, Software.

Declaration of competing interest

The authors declare that they have no known competing financial interests or personal relationships that could have appeared to influence the work reported in this paper.

Data availability

Data will be made available on request.

Acknowledgements

This work was financed by National Natural Science Foundation of China (NSFC Grant No.: 41974103) and a part of the Self-initiated project, modeling on the geodynamic subduction of the Pacific plate beneath the Changbaishan volcano since the Cenozoic, supported by the Institute of Geophysics, China Earthquake Administration. The improvement of this paper benefits from the critical and constructive comments as well as detailed suggestions provided by two anonymous reviewers and Editor Claire A. Currie. The numerical calculations in this paper were carried out on the ORISE Supercomputer and the Parallel Computing Platform of Institute of Geophysics, China Earthquake Administration. Most of Figures are generated using Generic Mapping Tools version 6 (Wessel et al., 2019).

Appendix A. Supplementary data

Supplementary data to this article can be found online at https://doi.org/10.1016/j.tecto.2024.230607.

References

Acocella, V., Di Lorenzo, R., Newhall, C., Scandone, R., 2015. An overview of recent (1988 to 2014) caldera unrest: knowledge and perspectives. Rev. Geophys. 53, 896–955.
Agrusta, R., Goes, S., van Hunen, J., 2017. Subducting-slab transition-zone interaction: stagnation, penetration and mode switches. Earth Planet. Sci. Lett. 464, 10–23.
Akaogi, M., Ito, E., 1993. Refinement of enthalpy measurement of $MgSiO_3$ perovskite and negative pressure-temperature slopes for perovskite-forming reactions. Geophys. Res. Lett. 20 (17), 1839–1842.
Akaogi, M., Ito, E., Navrotsky, A., 1989. Olivine-modified spinel-spinel transitions in the system Mg2SiO4-Fe2SiO4: calorimetric measurements, thermochemical calculation, and geophysical application. J. Geophys. Res. 94 (B11), 15671–15685.
Akaogi, M., Takayama, H., Kojitani, H., Kawaji, H., Atake, T., 2007. Low-temperature heat capacities, entropies and enthalpies of Mg_2SiO_4 polymorphs, and α-β-γ and post-spinel phase relations at high pressure. Phys. Chem. Miner. 34, 169–183.
An, M., Shi, Y., 2006. Lithospheric thickness of the Chinese continent. Phys. Earth Plant. Inter. 159, 257–266.
Androvičová, A., Čížková, H., van den Berg, A., 2013. The effects of rheological decoupling on slab deformation in the Earth's upper mantle. Stud. Geophys. Geod. 57 (3), 460–481.
Auer, L., Boschi, L., Becker, T.W., Nissen-Meyer, T., Giardini, D., 2014. Savani: a variable resolution whole-mantle model of anisotropic shear-velocity variations based on multiple datasets. J. Geophys. Res. 119, 3006–3034.
Behr, W.M., Holt, A.F., Becker, T.W., Faccenna, C., 2022. The effects of plate interface rheology on subduction kinematics and dynamics. Geophys. J. Int. 230, 796–812.
Benz, H.M., Vidale, J.E., 1993. Sharpness of upper-mantle discontinuities determined from high-frequency reflections. Nature 365, 147–150.
Billen, M.I., 2008. Modeling the dynamics of subducting slabs. Annu. Rev. Earth Planet. Sci. 36, 325–356.
Bina, C.R., Helffrich, G.R., 1994. Phase transition Clapeyron slopes and transition zone seismic discontinuity topography. J. Geophys. Res. 99, 15853–15960.
Bina, C.R., Stein, S., Marton, F.C., Van Ark, E.M., 2001. Implications of slab mineralogy for subduction dynamics. Phys. Earth Planet. Inter. 127, 51–66.
Capitanio, F.A., 2013. Lithospheric-age control on the migrations of oceanic convergent margins. Tectonophysics 593, 193–200.
Capitanio, F.A., Faccenda, C., 2012. Complex mantle flow around heterogeneous subducting oceanic plates. Earth Planet. Sci. Lett. 353–354, 29–37.
Capitanio, F., Morra, G., Goes, S., 2007. Dynamic models of downgoing plate-buoyancy driven subduction: subduction motions and energy dissipation. Earth Planet. Sci. Lett. 262, 284–297.
Carlson, R.L., Herrick, C.N., 1990. Densities and porosities in the oceanic crust and their variations with depth and age. J. Geophys. Res. 95, 9153–9170.
Carlson, R.L., Raskin, G.S., 1984. Density of the ocean crust. Nature 311, 555–558.
Castle, J.C., Creager, K.C., 2000. Local sharpness and shear wave speed jump across the 660-km discontinuity. J. Geophys. Res. 105 (B3), 6191–6200.
Cathles, L.M., 1975. The Viscosity of the Earth's Mantle. Princeton University Press, Princeton.
Chen, C., Zhao, D., Tian, Y., Wu, S., Hasegawa, A., Lei, J., Park, J., Kang, I., 2017. Mantle transition zone, stagnant slab and intraplate volcanism in Northeast Asia. Geophys. J. Int. 209, 68–85.
Chen, F., Davies, D.R., Goes, S., Suchoy, L., Kramer, S.C., 2022. How slab age and width combine to dictate the dynamics and evolution of subduction systems: a 3-D spherical study. Geochem. Geophys. Geosyst. 23. https://doi.org/10.1029/2022GC010597 e2022GC010597.
Chertova, M.V., Spakman, W., Steinberger, B., 2018. Mantle flow influence on subduction evolution. Earth Planet. Sci. Lett. 489, 258–266.
Chopelas, A., 1991. Thermal properties of β-Mg_2SiO_4 at mantle pressures derived from vibrational spectroscopy: implications for the mantle at 400 km depth. J. Geophys. Res. 96, 11817–11829.
Chopelas, A., Boehler, R., Ko, T., 1994. Thermodynamics and behavior of g-Mg_2SiO_4 at high pressure: implications for Mg_2SiO_4 phase equilibrium. Phys. Chem. Miner. 21, 351–359.
Christensen, U.R., 1996. The influence of trench migration on slab penetration into the lower mantle. Earth Planet. Sci. Lett. 140, 27–39.
Christensen, U.R., Yuen, D.A., 1984. The interaction of a subducting lithospheric slab with a chemical or phase boundary. J. Geophys. Res. 89, 4389–4402.
Christensen, U.R., Yuen, D.A., 1985. Layered convection induced by phase transitions. J. Geophys. Res. 90, 10291–10300.
Čížková, H., Bina, C.R., 2013. Effects of mantle and subduction-interface rheologies on slab stagnation and trench rollback, Earth planet. Sci. Lett. 379, 95–103.
Collier, J.D., Helffrich, G.R., Wood, B.J., 2001. Seismic discontinuities and subduction zones. Phys. Earth Planet. Inter. 127, 35–49.
Crameri, F., Lithgow-Bertelloni, C., 2018. Abrupt upper-plate tilting during slab-transition-zone collision. Tectonophysics 746, 199–211.
Crameri, F., Tackley, P.J., Meilick, I., Gerya, T.V., Kaus, B.J.P., 2012. A free plate surface and weak oceanic crust produce single-sided subduction on Earth. Geophys. Res. Lett. 39 (3). https://doi.org/10.1029/2011GL050046.
Davies, G.F., 1995. Penetration of plates and plumes through the mantle transition zone. Earth Planet. Sci. Lett. 133, 507–516.
Debayle, E., Dubuffet, F., Durand, S., 2016. An automatically updated S-wave model of the upper mantle and the depth extent of azimuthal anisotropy. Geophys. Res. Lett. 43, 674–682.
Deuss, A., 2009. Global observations of mantle discontinuities using SS and PP precursors. Surv. Geophys. 30 (4), 301–326.
Du, M., Lei, J., 2019. Pn anisotropy tomography of Northeast China and its implications to mantle dynamics. J. Asia Earth Sci. 171, 334–347.
Durand, S., Debayle, E., Richard, Y., Zaroli, C., Lambotte, S., 2017. Confirmation of a change in the global shear velocity pattern at around 1000 km depth. Geophys. J. Int. 211, 1628–1639.
Dziewonski, A.M., Anderson, D.L., 1981. Preliminary reference Earth model. Phys. Earth Planet. Inter. 25 (4), 297–356.
Estabrook, C.H., Kind, R., 1996. The nature of the 660-kilometer upper-mantle seismic discontinuity from precursors to the PP phase. Science 274 (5290), 1179–1182.
Faccenda, M., Capitanio, F.A., 2013. Seismic anisotropy around subduction zones: insights from three-dimensional modeling of upper mantle deformation and SKS splitting calculations. Geochem. Geophys. Geosyst. 14 (1), 243–262.
Fei, Y., Van Orman, J., Li, J., van Westrenen, W., Sanloup, C., Minarik, W., Hirose, K., Komabayashi, T., Walter, M., Funakoshi, K., 2004. Experimentally determined postspinel transformation boundary in Mg_2SiO_4 using MgO as an internal pressure standard and its geophysical implications. J. Geophys. Res. 109 (B02305). https://doi.org/10.1029/2003JB002562.
Forte, A.M., Mitrovica, J.X., 1996. New inferences of mantle viscosity from joint inversion of long-wavelength mantle convection and post-glacial rebound data. Geophys. Res. Lett. 23 (10), 1147–1150.
Forte, A.M., Mitrovica, J.X., 2001. Deep-mantle high-viscosity flow and thermochemical structure inferred from seismic and geodynamic data. Nature 410, 1049–1056.
Forte, A.M., Quéré, S., Moucha, R., Simmons, N.A., Grand, S.P., Mitrovica, J.X., Rowley, D.B., 2010. Joint seismic-geodynamic-mineral physical modelling of African geodynamics: a reconciliation of deep-mantle convection with surface geophysical constraints. Earth Planet. Sci. Lett. 295, 329–341.
French, S.W., Romanowicz, B.A., 2014. Whole-mantle radially anisotropic shear velocity structure from spectral-element waveform tomography. Geophys. J. Int. 199, 1303–1327.
Fukao, Y., Obayashi, M., 2013. Subducted slabs stagnant above, penetrating through, and trapped below the 660 km discontinuity. J. Geophys. Res. 118, 5920–5938.
Fukao, Y., Obayashi, M., Inoue, H., Nenbai, M., 1992. Subducting slabs stagnant in the mantle transition zone. J. Geophys. Res. 97, 4809–4822.

Fukao, Y., Obayashi, M., Nakakuki, T., 2009. Stagnant slab: a review. Annu. Rev. Earth Planet. Sci. 37, 19–46.
Funiciello, F., Faccenna, C., Giardini, D., 2004. Role of lateral mantle flow in the evolution of subduction systems: insights from laboratory experiments. Geophys. J. Int. 157 (3), 1393–1406.
Funiciello, F., Moroni, M., Piromallo, C., Faccenna, C., Cenedese, A., Bui, H.A., 2006. Mapping mantle flow during retreating subduction: laboratory models analyzed by feature tracking. J. Geophys. Res. 111. https://doi.org/10.1029/2005JB003792.
Garel, F., Goes, S., Davies, D.R., Davies, J.H., Kramer, S.C., Wilson, C.R., 2014. Interaction of subducted slabs with the mantle transition zone: a regime diagram from 2-D thermo-mechanical models with a mobile trench and an overriding plate. Geochem. Geophys. Geosyst. 15, 1739–1765.
Ghosh, S., Ohtani, E., Litasov, K.D., et al., 2013. Effect of water in depleted mantle on post-spinel transition and implication for 660 km seismic discontinuity. Earth Planet. Sci. Lett. 371-371, 103–111.
Griffiths, R.W., Hackney, R.I., Van Der Hilst, R.D., 1995. A laboratory investigation of effects of trench migration on the descent of subducted slabs. Earth Planet. Sci. Lett. 133 (1–2), 1–17. https://doi.org/10.1016/0012-821X(95)00027-A.
Guo, Z., Wang, K., Yang, Y., et al., 2018. The origin and mantle dynamics of quaternary intraplate volcanism in Northeast China from joint inversion of surface wave and body wave. J. Geophys. Res. 123, 2410–2425.
Gurnis, M., Turner, M., Zahirovic, S., DiCaprio, L., Spasojevic, S., Müller, R.D., Boyden, J., Seton, M., Manea, V.C., Bower, D.J., 2012. Plate tectonic reconstructions with continuously closing plates. Comput. Geosci. 38, 35–42.
Hager, B.H., 1984. Subducted slabs and the geoid: constraints on mantle rheology and flow. J. Geophys. Res. 89 (B7), 6003–6015.
Hager, B.H., Richards, M.A., 1989. Long-wavelength variations in earth's geoid: physical models and dynamical implications. Philos. Trans. R. Soc. Lond. A 328 (1599), 309.
Hager, B.H., Clayton, R.W., Richards, M.A., Comer, R.P., Dziewonski, A.M., 1985. Lower mantle heterogeneity, dynamic topography and the geoid. Nature 313, 541–545.
Hirose, K., 2002. Phase transitions in pyrolitic mantle around 670-km depth: implications for upwelling of plumes from the lower mantle. J. Geophys. Res. 107 (2078). https://doi.org/10.1029/2001JB000597.
Hong, H., Wu, J., Wang, Q., Li, K., Zhao, C., Shangguan, Z., Yang, Q., Zhang, H., Liu, G., 2007. Volcanic threat levels and classification of volcanic activity in China. Seismol. Geol. 29 (3), 447–458 (in Chinese).
Houser, C., Masters, G., Shearer, P., Laske, G., 2008. Shear and compressional velocity models of the mantle from cluster analysis of long-period waveforms. Geophys. J. Int. 174, 195–212.
Hu, J., Gurnis, M., 2020. Subduction duration and slab dip. Geochem. Geophys. Geosyst. 21. https://doi.org/10.1029/2019GC008862 e2019GC008862.
Hu, J., Liu, L., Hermosillo, A., Zhou, Q., 2016. Simulation of late Cenozoic South American flat-slab subduction using geodynamic models with data assimilation. Earth Planet. Sci. Lett. 438, 1–13.
Hu, J., Faccenda, M., Liu, L., 2017. Subduction-controlled mantle flow and seismic anisotropy in South America. Earth Planet. Sci. Lett. 470, 13–24.
Hu, J., Liu, L., Zhou, Q., 2018. Reproducing past subduction and mantle flow using high-resolution global convection models. Earth Planet. Phys. 2, 189–207.
Ita, J.J., King, S.D., 1994. The sensitivity of convection with an endothermic phase change to the form of governing equations, initial conditions, aspect ratio, and equation of state. J. Geophys. Res. 99, 15919–15938.
Ita, J.J., King, S.D., 1998. The influence of thermodynamic formulation on simulations of subduction zone geometry and history. Geophys. Res. Lett. 25, 1463–1466.
Ito, E., Takahashi, E., 1989. Postspinel transformations in the system Mg_2SiO_4–Fe_2SiO_4 and some geophysical implications. J. Geophys. Res. 94, 10637–10646.
Ito, E., Yamada, H., 1982. Stability relations of silicate spinels, ilmenites and perovskites. In: Akimoto, S., Maghnani, M.H. (Eds.), High-Pressure Research in Geophysics. Springer, The Netherlands, pp. 405–419.
Ito, E., Akaogi, M., Topor, L., Navrotsky, A., 1990. Negative pressure-temperature slopes for reactions forming $MgSiO_3$ perovskite from calorimetry. Science 249, 1275–1278.
Jackson, M.G., Konter, J.G., Becker, T.W., 2017. Primordial helium entrained by the hottest mantle plumes. Nature 000, 1–11.
Jiménez-Díaz, A., Ruiz, J., Villaseca, C., Tejero, R., Capote, R., 2012. The thermal state and strength of the lithosphere in the Spanish Central System and Tajo Basin from crustal heat production and thermal isostasy. J. Geodyn. 58, 29–37.
Kato, M., Kawakatsu, H., 2001. Seismological in situ estimation of density jumps across the transition zone discontinuities beneath Japan. Geophys. Res. Lett. 28 (13), 2541–2544.
Katsura, T., Ito, E., 1989. The system Mg_2SiO_4-Fe_2SiO_4 at high pressures and temperatures: precise determination of stabilities of olivine, modified spinel, and spinel. J. Geophys. Res. 94 (B11), 15663–15670.
Katsura, T., Yamada, H., Shinmei, T., Kubo, A., Ono, S., Kanzaki, M., Yoneda, A., Walter, M.J., Ito, E., Urakawa, S., Funakoshi, K., Utsumi, W., 2003. Post-spinel transition in Mg_2SiO_4 determined by high P-T in situ X-ray diffractometry. Phys. Earth Planet. Inter. 136, 11–24.
Kennett, B.L.N., Engdahl, E.R., 1991. Traveltimes for global earthquake location and phase identification. Geophys. J. Int. 105, 429–465.
Kennett, B.L.N., Engdahl, E.R., Buland, R., 1995. Constraints on seismic velocities in the Earth from traveltimes. Geophys. J. Int. 122, 108–124.
Kido, M., Yuen, D.A., Čadek, O., Nakakuki, T., 1998. Mantle viscosity derived by genetic algorithm using oceanic geoid and seismic tomography for whole-mantle versus blocked-flow situations. Phys. Earth Planet. Inter. 107 (4), 307–326.
Kincaid, C., Griffiths, R.W., 2003. Laboratory models of the thermal evolution of the mantle during rollback subduction. Nature 425, 58–62.
Kincaid, C., Olson, P., 1987. An experimental study of subduction and slab migration. J. Geophys. Res. 92 (13), 832–840.
King, S.D., 2007. Mantle downwellings and the fate of subducting slabs: Constraints from seismology, geoid, topography, geochemistry, and petrology. In: Bercovici, D. (Ed.), Treatise on Geophysics, Volume 7, Mantle Dynamics. Elsevier, Amsterdam, pp. 325–370.
King, S.D., Ita, J., 1995. Effect of slab theology on mass transport across a phase transition boundary. J. Geophys. Res. 100, 20211–20222.
King, S.D., Masters, G., 1992. An inversion for radial viscosity structure using seismic tomography. Geophys. Res. Lett. 19 (15), 1551–1554.
King, S.D., Frost, D.J., Rubie, D.C., 2015. Why cold slabs stagnate in the transition zone. Geology 43 (3), 231–234.
Király, Á., Portner, D.E., Haynie, K.L., Chilson-Parks, B.H., Ghosh, T., Jadamec, M., Makushkina, A., Manga, M., Moresi, L., O'Farrell, K.A., 2020. The effect of slab gaps on subduction dynamics and mantle upwelling. Tectonophysics 785, 228458.
Kojitani, H., Inoue, T., Akaogi, M., 2016. Precise measurements of enthalpy of postspinel transition in Mg_2SiO_4 and application to the phase boundary calculation. J. Geophys. Res. 121, 729–742.
Koulakov, I., 2011. High-frequency P and S velocity anomalies in the upper mantle beneath Asia from inversion of worldwide traveltime data. J. Geophys. Res. 116 (B04301). https://doi.org/10.1029/2010JB007938.
Kumar, R.R., Gordon, R.G., 2009. Horizontal thermal contraction of oceanic lithosphere: the ultimate limit to the rigid plate approximation. J. Geophys. Res. 114, B01403. https://doi.org/10.1029/2007JB005473.
Kustowski, B., Ekström, G., Dziewoński, A.M., 2008. The shear-wave velocity structure in the upper mantle beneath Eurasia. Geophys. J. Int. 174, 978–992.
Lau, H.C., Romanowicz, B., 2021. Constraining jumps in density and elastic properties at the 660 km discontinuity using normal mode data via the Backus-Gilbert method. Geophys. Res. Lett. 48 (9). https://doi.org/10.1029/2020GL092217 e2020GL092217.
Lebedev, S., Chevrot, S., van der Hilst, R.D., 2002. Seimic evidence for olivine phase changes at the 410- and 660-kilometer discontinuities. Sicence 296, 1300–1302.
Lei, J., Xie, F., Fan, Q., Santosh, M., 2013. Seismic imaging of the deep structure under the Chinese volcanos: an overview. Phys. Earth Plant. Inter. 224, 104–123.
Lekić, V., Romanowicz, B.A., 2011. Inferring upper-mantle structure by full waveform tomography with the spectral element method. Geophys. J. Int. 185, 799–831.
Li, C., van der Hilst, R.D., 2010. Structure of the upper mantle and transition zone beneath Southeast Asia from traveltime tomography. J. Geophys. Res. 115 (B07308). https://doi.org/10.1029/2009JB006882.
Li, C., van der Hilst, R.D., Engdahl, E.R., Burdick, S., 2008. A new global model for P wave speed variations in Earth's mantle. Geochem. Geophys. Geosyst. 9 (Q05018). https://doi.org/10.1029/2007GC001806.
Li, J., Wang, X., Wang, X., Yuen, D.A., 2013. P and SH velocity structure in the upper mantle beneath Northeast China: evidence for a stagnant slab in hydrous mantle transition zone. Earth Planet. Sci. Lett. 367, 71–81.
Li, Z., Di Leo, J.F., Ribe, N.M., 2014. Subduction-induced mantle flow, finite strain and seismic anisotropy: numerical modeling. J. Geophys. Res. 119 (6), 5052–5076.
Li, Z., Gerya, T., Connolly, J., 2019a. Variability of subducting slab morphologies in the mantle transition zone: Insight from petrological-thermomechanical modeling. Earth Sci. Rev. 196. https://doi.org/10.1016/j.earscirev.2019.05.018.
Li, S., Huang, J., Liu, Z., Zhang, Y., 2019b. Study on the mantle discontinuity structure beneath Northeast China with time-frequency phase-weighted stacks of ambient noise correlations. Geophys. J. Int. 218, 1490–1501.
Li, J., Chen, M., Ning, J., Bao, T., Maguire, R., Flanagan, M.P., Zhou, T., 2022. Contraining the 410-km discontinuity and slab structure in the Kuril subduction zone with triplication waveforms. Geophys. J. Int. 228, 729–743.
Litasov, K., Ohtani, E., Sano, A., Suzuki, A., Funakoshi, K., 2005a. Wet subduction versus cold subduction. Geophys. Res. Lett. 32 (L13312). https://doi.org/10.1029/2005GL022921.
Litasov, K., Ohtani, E., Sano, A., Suzuki, A., Funakoshi, K., 2005b. In situ X-ray diffraction study of post-spinel transformation in a peridotite mantle: implication for the 660-km discontinuity. Earth Planet. Sci. Lett. 238, 311–328.
Liu, L., Stegman, D.R., 2011. Segmentation of the Farallon slab. Earth Planet. Sci. Lett. 311, 1–10.
Liu, X., Zhong, S., 2016. Constraining mantle viscosity structure for a thermochemical mantle using the geoid observation. Geochem. Geophys. Geosyst. 17, 895–913.
Liu, L., Zhou, Q., 2015. Deep recycling of oceanic asthenosphere material during subduction. Geophys. Res. Lett. 42, 2204–2211.
Liu, J., Chen, S., Guo, W., Sun, C., Zhang, M., Guo, Z., 2015. Research advances in the Mt. Changbai volcano. Bull. Mineral. Petrol. Geochem. 34 (4), 710–723 (In Chinese).
Liu, H., Gurnis, M., Leng, W., 2021. Constraints on mantle viscosity from slab dynamics. J. Geophys. Res. 126. https://doi.org/10.1029/2021JB022329 e2021JB022329.
Lu, C., Grand, S.P., Lai, H., Garnero, E.J., 2019. TX2019slab: a new P and S tomography model incorporating subducting slabs. J. Geophys. Res. https://doi.org/10.1029/2019JB017448.
Ma, P., Liu, S., Gurnis, M., Zhang, B., 2019. Slab horizontal subduction and slab tearing beneath East Asia. Geophys. Res. Lett. 46 (10), 5161–5169.
Magni, V., Király, Á., 2019. Delamination. Environ. Sci, Earth syst. https://doi.org/10.1016/B978-0-12-409548-9.09515-4.
Mao, W., Zhong, S.J., 2018. Slab stagnation due to a reduced viscosity layer beneath the mantle transition zone. Nat. Geosci. 11, 876–881.
Matsui, M., 2001. Density and bulk sound velocity jumps across the 660 km seismic discontinuity. Phys. Earth Planet. Inter. 125 (1–4), 141–146.
Mitrovica, J.X., Forte, A.M., 1997. Radial profile of mantle viscosity: results from the joint inversion of convection and postglacial rebound observables. J. Geophys. Res. 102 (B2), 2751–2770.

Mitrovica, J.X., Forte, A.M., 2004. A new inference of mantle viscosity based upon joint inversion of convection and glacial isostatic adjustment data, Earth planet. Sci. Lett. 225, 177–189.
Mitrovica, J.X., Peltier, W.R., 1993. Present-day secular variations in the zonal harmonics of the Earth's geopotentiaI. J. Geophys. Res. 98, 4509–4526.
Mitrovica, J.X., Peltier, W.R., 1995. Constraints on mantle viscosity based upon the inversion of post-glacial uplift data from the Hudson Bay region. Geophys. J. Int. 122, 353–377.
Montagner, J.-P., Anderson, D.L., 1989. Constrained reference mantle model. Phys. Earth Planet. Inter. 58 (2–3), 205–227.
Morelli, A., Dziewonski, A.M., 1993. Body wave traveltimes and a spherically symmetric P- and S-wave velocity model. Geophys. J. Int. 112 (2), 178–194.
Moresi, L., Zhong, S., Gurnis, M., 1996. The accuracy of finite element solutions of Stokes's flow with strongly varying viscosity. Phys. Earth Planet. Inter. 97, 83–94.
Morgan, J.P., Hasenclever, J., Hort, M., Rüpke, L., Parmentier, E.M., 2007. On subducting slab entrainment of buoyant asthenosphere. Terra Nova 19, 167–173.
Morishima, H., Kato, T., Suto, M., Ohtani, E., Urakawa, S., Utsumi, W., Shimomura, O., Kikegawa, T., 1994. The phase boundary between α- and β-Mg_2SiO_4 determined by in Situ X-ray observation. Science 265, 1202–1203.
Müller, R.D., Seton, M., Zahirovic, S., Williams, S.E., Matthews, K.J., Wright, N.M., Shephard, G.E., Maloney, K.T., Barnett-Moore, N., Hosseinpour, M., Bower, D.J., Cannon, J., 2016. Ocean basin evolution and global-scale plate reorganization events since pangea breakup. Annu. Rev. Earth Planet. Sci. 44, 107–138.
Nakada, M., Lambeck, K., 1989. Late Pleistocene and Holocene Sea-level change in the Australian region and mantle rheology. Geophys. J. Int. 96, 497–517.
Obayashi, M., Yoshimitsu, J., Nolet, G., Fukao, Y., Shiobara, H., Sugioka, H., Miyamachi, H., Gao, Y., 2013. Finite frequency whole mantle P wave tomography: Improvement of subducted slab images. Geophys. Res. Lett. 40, 5652–5657.
Panning, M.P., Lekić, V., Romanowicz, B.A., 2010. Importance of crustal corrections in the development of a new global model of radial anisotropy. J. Geophys. Res. 115 (B12325). https://doi.org/10.1029/2010JB007520.
Paulson, A., Zhong, S., Wahr, J., 2007. Inference of mantle viscosity from GRACE and relative sea level data. Geophys. J. Int. 171, 491–508.
Peng, D., Liu, L., Hu, J., Li, S., Liu, M., 2021a. Formation of east Asian stagnant slabs due to a pressure-driven Cenozoic mantle wind following Mesozoic subduction. Geophys. Res. Lett. 48 (18). https://doi.org/10.1029/2021GL094638 e2021GL094638.
Peng, D., Liu, L., Wang, Y., 2021b. A newly discovered Late-cretaceous East Asian flat slab explains its unique lithospheric structure and tectonics. J. Geophys. Res. 126 (10) e2021JB022103.
Petersen, N., Vinnik, L., Kosarev, G., Kind, R., Oreshin, S., Stammler, K., 1993. Sharpness of the mantle discontinuities. Geophys. Res. Lett. 20 (9), 859–862.
Pokorny, J., Čížková, H., van den Berg, A., 2021. Feedbacks between subduction dynamics and slab deformation: combined effects of nonlinear rheology of a weak decoupling layer and phase transitions. Phys. Earth Planet. Inter. 313. https://doi.org/10.1016/j.pepi.2021.106679.
Ratnaswamy, V., Stadler, G., Gurnis, M., 2015. Adjoint-based estimation of plate coupling in a non-linear mantle flowmodel: theory and examples. Geophys. J. Int. 202 (2), 768–786.
Revenaugh, J., Jordan, T.H., 1991. Mantle layering from ScS reverberations 2. The transition zone. J. Geophys. Res. 96 (B12), 19763–19780.
Ribe, N.M., 2010. Bending mechanics and mode selection in free subduction: a thin-sheet analysis. Geophys. J. Int. 180, 559–576.
Ricard, Y., Bai, W., 1991. Inferring viscosity and the 3-D density structure of the mantle from geoid, topography and plate velocities. Geophys. J. Int. 105, 561–572.
Ricard, Y., Richards, M., Lithgow-Bertelloni, C., Le Stunff, Y., 1993. A geodynamic model of mantle density heterogeneity. J. Geophys. Res. 98 (B12), 21895–21909.
Ringwood, A.E., 1969. Phase transformations in the mantle. Earth Planet. Sci. Lett. 5, 401–412.
Ritsema, J., Deuss, A., van Heijst, H.J., Woodhouse, J.H., 2011. S40RTS: a degree-40 shear-velocity model for the mantle from new Rayleigh wave dispersion, teleseismic traveltime and normal-mode splitting function measurements. Geophys. J. Int. 184, 1223–1236.
Rudolph, M.L., Moulik, P., Lekić, V., 2020. Bayesian inference of mantle viscosity from whole-mantle density models. Geochem. Geophys. Geosyst. 21. https://doi.org/10.1029/2020GC009335 e2020GC009335.
Sharples, W., Jadamec, M.A., Moresi, L.N., Capitanio, F.A., 2014. Overriding plate controls on subduction evolution. J. Geophys. Res. 119, 6684–6704.
Shearer, P.M., Flanagan, M.P., 1999. Seismic velocity and density jumps across the 410- and 660-kilometer discontinuities. Science 285 (5433), 1545–1548.
Sheng, J., Liao, J., Li, Y., Hu, Q., Xu, L., Zhou, Z., 2018. Influence of the Pacific plate subduction on the Tianchi volcano. Chin. J. Geophys. 61 (11), 4396–4405 (In Chinese).
Simmons, N.A., Forte, A.M., Boschi, L., Grand, S.P., 2010. GyPSuM: a joint tomographic model of mantle density and seismic wave speeds. J. Geophys. Res. 115 (B12310). https://doi.org/10.1029/2010JB007631.
Simmons, N.A., Myers, S.C., Johannesson, G., Matzel, E., 2012. LLNL-G3Dv3: Global P wave tomography model for improved regional and teleseismic travel time prediction. J. Geophys. Res. 117, B10302. https://doi.org/10.1029/2012JB009525.
Solheim, L.P., Peltier, W.R., 1994a. Phase boundary deflections at 660 km depth and episodically layered isochemical convection. J. Geophys. Res. 99 (15), 861–875.
Solheim, L.P., Peltier, W.R., 1994b. Avalanche effects in phase transition modulated thermal convection: a model for the Earth's mantle. J. Geophys. Res. 99, 6997–7018.
Stegman, D.R., Farrington, R., Capitanio, F.A., Schellart, W.P., 2010. A regime diagram for subduction styles from 3-D numerical models of free subduction. Tectonophysics 483, 29–45.
Steinbach, V., Yuen, D.A., 1992. The effects of multiple phase transitions on Venusian mantle convection. Geophys. Res. Lett. 19, 2243–2246.
Steinberger, B., Calderwood, A.R., 2006. Models of large-scale viscous flow in the Earth's mantle with constraints from mineral physics and surface observations. Geophys. J. Int. 167, 1461–1481.
Tackley, P.J., Stevenson, D.J., Glatzmaier, G.A., Schubert, G., 1993. Effects of an endothermic phase transition at 670 km depth on spherical mantle convection. Nature 361, 699–704.
Tackley, P.J., Stevenson, D.J., Glatzmaier, G.A., Schubert, G., 1994. Effects of multiple phase transitions in a three-dimensional spherical model of convection in Earth's mantle. J. Geophys. Res. 99 (15), 877–901.
Tan, E., Choi, E., Thoutireddy, P., Gurnis, M., Aivazis, M., 2006. GeoFramework: Coupling multiple models of mantle convection within a computational framework. Geochem. Geophys. Geosyst. 7 (Q06001). https://doi.org/10.1029/2005GC001155.
Tang, J., Zhao, G., Wang, J., Zhan., Y., Deng, Q., Chen, X., 2006. Study of the formation mechanism for volcanism in Northeast China based on deep electric structure. Acta Petrol. Sin. 22 (6), 1503–1510 (in Chinese).
Tang, Y., Obayashi, M., Niu, F., Grand, S.P., Chen, Y., Kawakatsu, H., Tanaka, S., Ning, J., Ni, J., 2014. Changbaishan volcanism in Northeast China linked to subduction-induced mantle upwelling. Nat. Geosci. 7, 470–475.
Tao, K., Grand, S.P., Niu, F., 2018. Seismic structure of the upper mantle beneath eastern Asia from full waveform seismic tomography. Geochem. Geophys. Geosyst. 19, 2732–2763.
Tian, Y., Zhu, H., Zhao, D., Liu, C., Feng, X., Liu, T., Ma, J., 2016. Mantle transition zone structure beneath the Changbai volcano: Insight into deep slab dehydration and hot upwelling near the 410 km discontinuity. J. Geophys. Res. 121, 5794–5808.
Tibi, R., Wiens, D.A., 2005. Detailed structure and sharpness of upper mantle discontinuities in the Tonga subduction zone from regional broadband arrays. J. Geophys. Res. 110 (B06313B6). https://doi.org/10.1029/2004JB003433.
Turcotte, D., Schubert, G., 2014. Geodynamics, Third edition. Cambridge University Press, pp. 189–193.
Tushingham, A.M., Peltier, W.R., 1992. Validation of the ICE-3G model of Würm-Wisconsin deglaciation using a global data base of relative sea level histories. J. Geophys. Res. 97, 3285–3304.
Vinnik, L., Deng, Y., Kosarev, G., Oreshin, S., Zhang, Z., Makeyeva, L., 2020. Sharpness of the 410-km discontinuity from P410s and P2p410s seismic phases. Geophys. J. Int. 220, 1208–1214.
Wang, L., He, X., 2020. Sharpness of the paired 660-km discontinuity beneath the Izu-Bonin area. Earth Planet Phys. 4 (6), 627–638.
Wang, B., Niu, F., 2010. A broad 660-km discontinuity beneath Northeast China revealed by dense regional seismic networks in China. J. Geophys. Res. 115 (B06308). https://doi.org/10.1029/2009JB006608.
Wang, J., Gu, Y.J., Schmerr, N., 2023. Global variability of density contrast across the 660-km discontinuity. Geophys. Res. Lett. 50. https://doi.org/10.1029/2022GL101213 e2022GL101213.
Wei, W., Xu, J., Zhao, D., Shi, Y., 2012. East Asia mantle tomography: new insight into plate subduction and intraplate volcanism. J. Asian Earth Sci. 60, 88–103.
Wei, H., Liu, G., Gill, J., 2013. Review of eruptive activity at Tianchi volcano, Changbaishan, Northeast China: Implications for possible future eruptions. Bull. Volcanol. 75 (4), 1–14.
Wei, W., Zhao, D., Xu, J., Wei, F., Liu, G., 2015. P and S wave tomography and anisotropy in Northwest Pacific and East Asia: Constraints on stagnant slab and intraplate volcanism. J. Geophys. Res. 120, 1642–1666.
Wessel, P., Luis, J.F., Uieda, L., Scharroo, R., Wobbe, F., Smith, W.H.F., Tian, D., 2019. The Generic Mapping Tools version 6. Geochem. Geophys. Geosyst. 20, 5556–5564.
Wu, P., Peltier, W.R., 1983. Glacial isostatic adjustment and the free air gravity anomaly as a constraint on deep mantle viscosity. Geophys. J. R. Astron. Soc. 74, 377–450.
Wu, J., Ming, Y., Zhang, H., Liu, G., Fang, L., Su, W., Wang, W., 2007. Earthquake swarm activity in Changbaishan Tianchi volcano. Chin. J. Geophys. 50 (4), 1089–1096 (in Chinese).
Xu, F., Vidale, J.E., Earle, P.S., 2003. Survey of precursors to P'P': Fine structure of mantle discontinuities. J. Geophys. Res. 108 (B1), 1–7.
Xu, J., Liu, G., Wu, J., Ming, Y., Wang, Q., Cui, D., Shangguan, Z., Pan, B., Lin, X., Liu, J., 2012. Recent unrest of Changbaishan volcano, Northeast China: a precursor of a future eruption? Geophys. Res. Lett. 39 (L16305). https://doi.org/10.1029/2012GL052600.
Xue, K., Schellart, W.P., Strak, V., 2020. Effect of plate length on subduction kinematics and slab geometry: Insights from buoyancy-driven analog subduction models. J. Geophys. Res. 125. https://doi.org/10.1029/2020JB02051 e2020JB020514.
Yamazaki, A., Hirahara, K., 1994. The thickness of upper mantle discontinuities, as inferred from short-period J-array data. Geophys. Res. Lett. 21 (17), 1811–1814.
Yanagisawa, T., Yamagishi, Y., 2005. Rayleigh-Benard convection in spherical shell with infinite Prandtl number at high Rayleigh number. J. Earth Simul. 4, 11–17.
Yang, T., Moresi, L., Zhao, D., Sandiford, D., Whittaker, J., 2018. Cenozoic lithospheric deformation in Northeast Asia and the rapidly-aging Pacific Plate. Earth Planet. Sci. Lett. 492, 1–11.
Ye, L., Li, J., Tseng, T., Yao, Z., 2011. A stagnant slab in a water-bearing mantle transition zone beneath Northeast China: Implications from regional SH waveform modeling. Geophys. J. Int. 186, 706–710.
Yu, C., Day, E.A., de Hoop, M.V., Capillo, M., Goes, S., Blythe, R.A., van der Hilst, R.D., 2018. Compositional heterogeneity near the base of the mantle transition zone beneath Hawaii. Nat. Comm. 9 (1), 1–9.
Zhang, M., Sun, D., Wang, Y., Wu, Z., 2019. Fine structure of the 660-km discontinuity beneath southeastern China. Geophys. Res. Lett. 46, 7304–7314.
Zhao, W., Yuen, D.A., Honda, S., 1992. Multiple phase transitions and the style of mantle convection. Phys. Earth Planet. Inter. 72, 185–210.

Zhao, D., Isozaki, Y., Maruyama, S., 2017. Seismic imaging of the Asian orogens and subduction zones. J. Asian Earth Sci. 145, 349–367.
Zhong, S., Gurnis, M., 1994. Role of plates and temperature-dependent viscosity in phase change dynamics. J. Geophys. Res. 99, 15903–15917.
Zhong, S.J., Gurnis, M., 1995. Mantle convection with plates and mobile, faulted plate margins. Science 267, 838–843.
Zhong, S., Gurnis, M., 1997. Dynamic interaction between tectonic plates, subducting slabs, and the mantle. Earth Interact. 1 (3), 1–18.
Zhong, X., Li, Z., 2020. Subduction initiation during collision-induced subduction transference: Numerical modeling and implications for the Tethyan evolution. J. Geophys. Res. 125 (2). https://doi.org/10.1029/2019JB019288.
Zhong, S., Zuber, M.T., Moresi, L., Gurnis, M., 2000. Role of temperature-dependent viscosity and surface plates in spherical shell models of mantle convection. J. Geophys. Res. 105 (11), 11063–11082.
Zhong, S., McNamara, A., Tan, E., Moresi, L., Gurnis, M., 2008. A benchmark study on mantle convection in a 3-D spherical shell using CitcomS. Geochem. Geophys. Geosyst. 9 (Q10017). https://doi.org/10.1029/2008GC002048.
Zhu, T., 2014. Tomography-based mantle flow beneath Mongolia-Baikal area. Phys. Earth Planet. Inter. 237, 40–50.
Zhu, T., Peng, D., Liu, L., 2024. Effects of 410- and 660-km seismic discontinuities on the Pacific plate subduction and slab geometry beneath the Changbaishan volcanic province. Acta Seismol. Sin., doi:10.11939/jass.20240022 (accepted (in Chinese).
Zou, Y., 2018. Characteristics of 410- and 660-Km Discontinuities Inferred from P'P' Precursors. Master's thesis,. Zhejiang University (in Chinese).